Journal Pre-proof

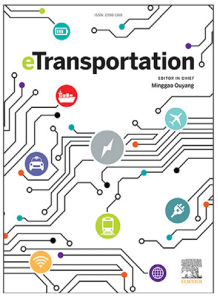

Efficient physics-based modeling and experimental validation of parallel-connected battery cells enabled by the transmission line model

Pablo Rodríguez-Iturriaga, Salvador Rodríguez-Bolívar, Simona Onori, Juan Antonio López-Villanueva

PII: S2590-1168(26)00041-X
DOI: https://doi.org/10.1016/j.etran.2026.100583
Reference: ETRAN 100583

To appear in: *eTransportation*

Received date : 10 October 2025
Revised date : 27 February 2026
Accepted date : 18 March 2026

Please cite this article as: P. Rodríguez-Iturriaga, S. Rodríguez-Bolívar, S. Onori et al., Efficient physics-based modeling and experimental validation of parallel-connected battery cells enabled by the transmission line model. *eTransportation* (2026), doi: https://doi.org/10.1016/j.etran.2026.100583.

Graphical Abstract

Efficient physics-based modeling and experimental validation of parallel-connected battery cells enabled by the transmission line model

Pablo Rodríguez-Iturriaga [1] , Salvador Rodríguez-Bolívar [2] , Simona Onori, Juan Antonio López-Villanueva

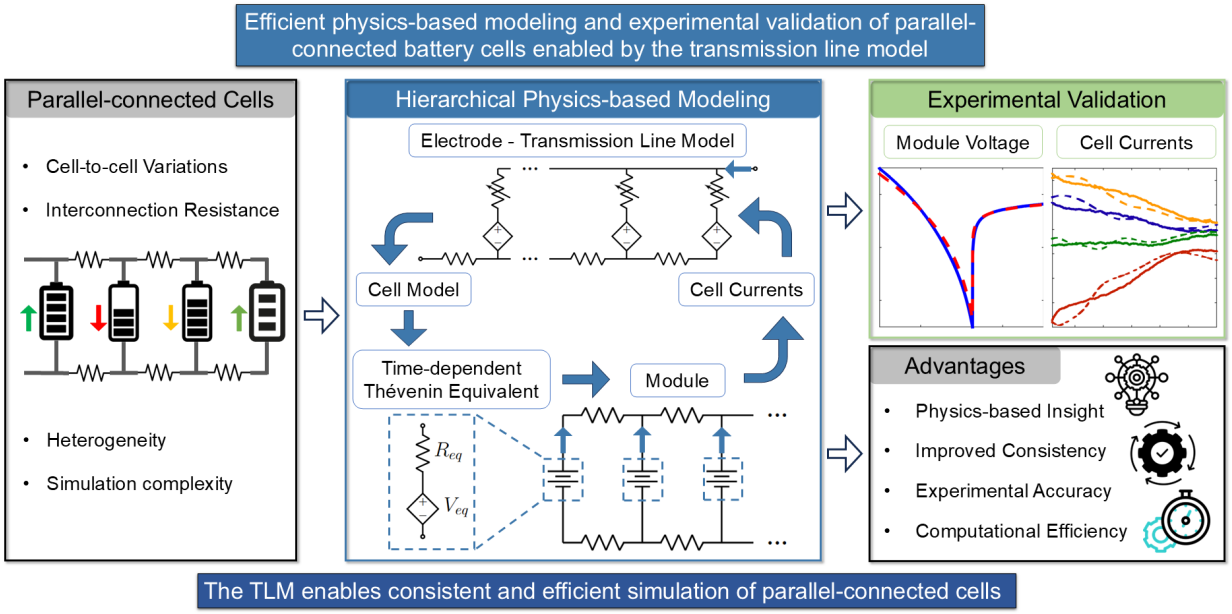

[1]Corresponding Author: priturriaga@ugr.es
[2]Corresponding Author: rbolivar@ugr.es

Highlights

Efficient physics-based modeling and experimental validation of parallel-connected battery cells enabled by the transmission line model

Pablo Rodríguez-Iturriaga [3] , Salvador Rodríguez-Bolívar [4] , Simona Onori, Juan Antonio López-Villanueva

- Physically motivated efficient simulation framework for parallel-connected cells
- Determination of a cell's electrically consistent equivalent voltage and resistance
- Accurate results for module voltage ($\leq$20mV RMS) and current distribution ($\leq$4.4% RMS)
- Experimental validation covering a wide range of operating scenarios
- Improved consistency and computational cost with respect to established approaches

[3]Corresponding Author: priturriaga@ugr.es
[4]Corresponding Author: rbolivar@ugr.es

Efficient physics-based modeling and experimental validation of parallel-connected battery cells enabled by the transmission line model

Pablo Rodríguez-Iturriaga [1] [a], Salvador Rodríguez-Bolívar [2] [a], Simona Onori[b], Juan Antonio López-Villanueva[a]

[a] *Department of Electronics and Computer Technology, University of Granada, Granada, 18071, Andalusia, Spain*
[b] *Department of Energy Science and Engineering, Stanford University, Stanford, 94305, California, USA*

Abstract

Battery modules composed of parallel-connected cells are commonly used as building blocks of battery packs, but their behavior is complex due to cell dynamics, as well as cell-to-cell heterogeneities and interactions. Furthermore, their simulation by means of empirical equivalent circuit models poses limitations because of lack of generalization, whereas electrochemical models lead to a challenging calculation of the current distribution. In this article, an electrically consistent method for the calculation of the equivalent voltage and resistance of a cell is presented according to the physically motivated discrete transmission line model. This enables the efficient computation of output voltage and current distribution for parallel-connected cells while providing interpretable physical information about the operation at each level. The presented approach is validated experimentally against a dataset of a 4P

[1] Corresponding Author: priturriaga@ugr.es
[2] Corresponding Author: rbolivar@ugr.es

module in which interconnection resistance, ambient temperature, and the presence of an aged cell are considered as input parameters, with accurate and consistent results for module voltage (≤20 mV RMS) and current distribution (≤4.4% RMS). Moreover, the proposed framework exhibits higher computational efficiency and comparable scalability in relation to established approaches, while providing improved consistency between module-level behavior and cell-level dynamics. Therefore, the proposed method based on the transmission line model and hierarchical simplification is a suitable alternative for the physically motivated simulation and analysis of battery modules.

Keywords: Lithium-ion battery, Parallel connection, Battery module, Transmission line model, Silicon-Graphite

1. Introduction

Lithium-ion batteries (LIBs) play a central role in transportation electrification [1]. As a result of energy and power requirements, large battery packs comprising hundreds to thousands of individual cells are utilized [2, 3]. Battery strings composed of parallel-connected cells are commonly employed as the building blocks of large battery packs due to advantages in available capacity, reliability [4, 5] and robustness [6]. For this reason, the study of parallel-connected cells constitutes an essential line of research for the adequate management of battery modules and packs [7, 8]. Nevertheless, the modeling and analysis of the behavior of parallel-connected cells is more complex than that of individual cells due to non-uniform real-world operation caused by cell dynamics, as well as cell-to-cell heterogeneities and interactions [9].

A detailed overview of the origins of cell-level parameter variations, their cross-interaction, and their resulting effects is provided in [10]. At the cell level, tolerances and inconsistencies in the manufacturing processes lead to fluctuations in capacity, AC impedance, DC resistance, and rate capability among cells in the same batch [11, 12], whose experimental characterization has been the subject of study in previous works [13, 14]. At the module level, assembly choices are also a source of non-uniform cell behavior: non-negligible interconnection [15] and contact resistances [16] influence the current distribution and rate capability of the module [17], therefore making the connection topology a relevant factor as well [18, 19]. Furthermore, the design of the cooling and thermal management systems [20, 21] can result in heterogeneous heat transfer characteristics between cells [22, 23]. As a result, both cell-level and module-level effects, as well as their interrelation, cause imbalances in stress factors such as C-rate, depth of discharge and temperature increase [24, 25, 26, 27], which in turn may lead to uneven cell degradation [28] and decrease in module performance [29]. Therefore, the development of high-fidelity models for the efficient simulation of battery modules constitutes a crucial line of research for an improved and quantitative understanding of non-uniform behavior at the cell level as well as its impact on module performance.

Since a module composed of the interconnection of several battery cells can be represented by a higher-level circuit network, most works that attempt to recreate the operation of battery modules make use of equivalent circuit models (ECMs) to emulate cell behavior due to simpler integration into the former. In particular, ECMs composed of an Open Circuit Volt-

age (OCV) source and a series resistance, and optionally several parallel resistor-capacitor (RC) networks, have been widely employed for the analytical calculation of the current distribution in ideal parallel-connected modules by means of suitable mathematical transformations [30, 31], as well as its experimental validation in some instances for a 2-parallel (2P) system [32, 33, 34]. This approach may be extended for the development of state observers for the estimation of individual cell variables, such as state of charge (SOC) [35, 36, 37]; it is also the basis for the simulation of larger battery packs to analyze the influence of pack topology [38, 39], current imbalances [29, 40] or statistical parameter distribution [41, 42] on pack performance, as well as experimental validation at a larger scale [3, 16]. The modeling of temperature distribution and the effect of cooling system design are also considered in some instances [22]. Additionally, the effect of interconnection and contact resistances may easily be incorporated within this approach, whose impact on the current distribution [19] as well as the state of available power [43] have recently been emphasized. However, standard ECMs, despite acceptable accuracy within certain operating regimes, lack a connection to the underlying physical processes [44] and require empirical dependencies of electrical parameters with SOC, which are major factors influencing the current distribution along with the nonlinearities in the shape of the OCV curve [24, 33]. As a result, their generalization ability is limited by the span of the experimental data used to calibrate them [3], and thus, a more general and physically motivated modeling approach for the simulation and validation of battery modules is desirable.

In contrast, fewer approaches in the literature employ electrochemical

models for the analysis of the behavior of parallel-connected cells because of the challenge of interfacing them with the circuit network representing the module [45]. In this regard, a thermally coupled Single Particle Model (SPM) was embedded into MATLAB-Simulink for the simulation of a 6P module in [46], including the effect of the contact and interconnection resistances. In [47], Padé approximations were employed to simplify the transcendental transfer functions obtained from the SPM with electrolyte (SPMe), which were then integrated into a Simulink submodel for module simulation. In the two previous cases, the coupling between behaviors at cell and module levels was not implemented explicitly and was handled by the Simulink solver. Some authors have also suggested employing an electrochemical model for internal cell dynamics, but replacing it by an equivalent circuit for an efficient calculation of module voltage and current distribution. In [48], a thermally coupled Doyle-Fuller-Newman (DFN) model is employed, but the current distribution is solved by substituting each cell by an equivalent circuit composed of an OCV voltage source in series with a polarization resistance calculated from simulated galvanostatic discharges. However, it was pointed out that this approach is not fully electrically consistent and is only adequate in steady state. The authors in [49] also employ a thermally coupled DFN model, solved in COMSOL, for the simulation of a 5P module including interconnection and contact resistances, with the coupling being implemented via MATLAB. In this case, the equivalent resistance is calculated from the difference between the terminal voltage given by the electrochemical model and the OCV corresponding to the SOC of each cell. A similar approach is implemented in `liionpack` [50], a software package for the simulation of

battery modules employing the cell models available in PyBaMM [51] within a circuit network symbolizing the module. Nevertheless, if the equivalent resistance is calculated as the ratio between cell overpotential and current, it is implicitly assumed that the former is fully ohmic in nature, which is not completely consistent with the internal dynamics of the electrochemical model and may overestimate instantaneous cell resistance. Furthermore, this approach leads to numerical instability during relaxation, since the resulting equivalent resistance may take unphysical values as currents approach zero or change direction during module rebalancing. For this reason, the determination of an electrically consistent equivalent circuit from an electrochemical model remains an open question.

In summary, the following gaps are identified in the literature regarding the simulation and experimental validation of parallel-connected cells:

- Most of the literature on the modeling and analysis of parallel-connected cells has employed empirical ECMs, with interconnection and contact resistances often being omitted.
- Electrochemical models lead to a complex computation of the current distribution, and the method for calculating their equivalent circuit in an electrically consistent manner has not been adequately addressed.
- The experimental validation of module voltage has received substantially less attention than that of the current distribution.

For the reasons above, an accurate physics-based cell model is required, which allows for a consistent computation of its equivalent voltage and resistance for an efficient simulation of the parallel connection of several cells.

In a previous work [52], we developed a physics-based ECM for a commercial Nickel-Maganese-Cobalt/Silicon-Graphite (NMC/Si-Gr) cell based on the transmission line model (TLM), with the key difference of a discrete instead of continuous spatial distribution of active material particles within the electrode. We showed that an optimal number of particles, along with a macroscale ohmic resistance and a particle size distribution for graphite, were required to reproduce cell voltage at increasing C-rates as well as the subsequent relaxation with a single set of parameters. In this article, we introduce the hierarchical procedure to integrate this model within a parallel module for an efficient simulation and experimental validation of module behavior in a variety of operating scenarios. To the best of our knowledge, this is the first time the circuit formulation of the TLM has been leveraged for the electrically consistent calculation of equivalent voltage and resistances, leading to an efficient computation of module voltage and current distribution.

The main contributions of this article are summarized as follows:

- A novel hierarchical simulation framework for parallel-connected cells is presented based on the physically motivated discrete transmission line cell model and the calculation of electrically consistent values of equivalent voltages and resistances.

- Module voltage and current distribution are simultaneously validated with high accuracy against an experimental dataset in which the interconnection resistance, ambient temperature, and the presence or absence of an aged cell are considered as input parameters.

- The presented methodology is assessed in relation to established ap-

proaches for the physically motivated simulation of battery modules, as well as the usage of traditional ECMs for this purpose.

The outline of this paper is the following: the employed cell model is described in Section 2, and the procedure for module simulation is presented in Section 3. The proposed approach is validated and discussed in Section 5 with the aid of the experimental dataset described in 4. Some concluding remarks are provided in Section 6.

2. Transmission line cell model

In a previous work [52], we developed and validated a physics-based equivalent circuit model ECM for a NMC/Si-Gr cell following the TLM approach (see Fig. 1). The application of TLMs to porous electrode modeling was first presented by De Levie as a method for the description of their impedance response [53], on which several authors have subsequently elaborated [54, 55]. The TLM approach may also be employed for time-domain simulations as a physically motivated equivalent circuit of the standard DFN model [56, 57], as demonstrated in [58, 44]. As the authors in [44] provide a detailed derivation of the electrical equivalence of each physical process, herein only a brief overview is included, along with the key differences with their approach.

- **Solid diffusion.** The auxiliary subcircuits in Fig. 1-b) model the solid diffusion process within active material particles by approximating the transfer function associated with this process (see Eq. 1) by electrical elements and providing both average and surface concentrations, thus reducing the number of states required. The surface concentrations are

used to evaluate the Open Circuit Potential (OCP) function, represented by controlled voltage sources in Fig. 1-a). It is noted that there is one subcircuit per spatial node, so intercalation currents are local. This process is determined by electrode capacities Q_P, Q_N and time constants $\tau_{d,NMC}, \tau_{d,Si}, \tau_{d,Gr}$. In the case of graphite, $\tau_{d,Gr,ref}$ is multiplied by the ratio of particle sizes to obtain individual time constants.

- **Charge transfer.** Charge transfer overpotentials are modeled by nonlinear charge transfer resistances (see Eq. 3) depending on the local intercalation current and the local exchange current (see Eq. 4). This process is determined by the exchange currents $K_{0,NMC}, K_{0,Si}, K_{0,Gr}$.

- **Electronic transport in the solid.** This process is accounted for by means of distributed resistors on the outer rails that model ohmic losses in the solid [58, 44]. However, since electronic conductivity is usually several orders of magnitude larger than ionic conductivity [59], its effect may be safely neglected without compromising accuracy. As a result, solid potential does not depend on spatial position, which facilitates simulation as well as the application of circuit network simplifications.

- **Ionic transport in the electrolyte.** This process is commonly split into two components: ohmic losses are modeled by distributed resistances on the inner rails $R_{ohm,PE}$ and $R_{ohm,NE}$, whereas several approaches exist to account for ionic diffusion within this modeling framework. Some authors include additional controlled voltage sources to account for the overpotential due to concentration gradients [58, 44], while others include a second transmission line on the electrolyte rail

[55]. In this work, all the electrolyte effects are combined in the ohmic resistances $R_{ohm,PE}$ and $R_{ohm,NE}$ due to the challenge posed by the separate identification of these two mechanisms from experimental data.

The main distinction of the model in Fig. 1 from a standard TLM lies in a discrete spatial distribution described by a finite number of particles within each electrode N_{PE}, N_{NE} and a macroscale ohmic resistance R_{ohm}, instead of a continuous spatial structure with a large number of nodes N and a distributed resistance R_{ohm}/N [55]. This assumption is based on the fact that a continuous spatial geometry may not be the most suitable description of electrode spatial structure [60], since active material particles are not microscale with respect to electrode thickness for this chemistry as reported in [59]. We have shown in previous works [61, 62] that a discrete spatial structure is also more consistent with EIS spectra, as the ohmic resistance is interpreted as the resistance between particles instead of a lumped element.

This modeling framework allows for the simplified inclusion of silicon particles, as well as a particle size distribution for graphite (3 sizes shown in Fig. 1), by defining additional branches in each spatial node. As a result of these considerations, the model is able to provide highly accurate results upon validation against experimental data at different C-rates with a single set of constant parameters. In particular, we showed that $N_{PE} = 6, N_{NE} = 6$ allows reproducing the slope of cell voltage during galvanostatic discharges due to increasingly sequential operation [52], while a particle size distribution for graphite contributed decisively to matching relaxation profiles after discharge. This approach presents two key advantages: first, only electrical parameters are required instead of all the physical parameters of an electro-

chemical model, and second, the TLM formulation enables the application of circuit network simplifications, which enable an efficient hierarchical simulation of parallel-connected cells.

Given that the profiles employed for experimental validation in this work are discharges followed by relaxation, we have employed delithiation OCPs for both silicon and graphite. The presented modeling framework also enables the separate simulation of module charging by making use of lithiation OCPs, as illustrated in Fig. S1. Nevertheless, the implementation of the cell-level switching between lithiation and delithiation OCPs in dynamic operating conditions at the module level poses a significant challenge due to inherent numerical instability and potentially inconsistent results. We have verified that a sigmoid function of instantaneous cell current, as in [63], results in numerical divergence at the module level in several common operating scenarios. We believe that the current understanding of hysteresis and present modeling alternatives are not sufficient to properly address dynamic operation at the module level while taking into account the transient component of cell-level hysteresis. However, we understand that this limitation is not exclusive to this modeling approach, and we identify this issue as the key challenge for a comprehensive understanding of the behavior of parallel-connected cells.

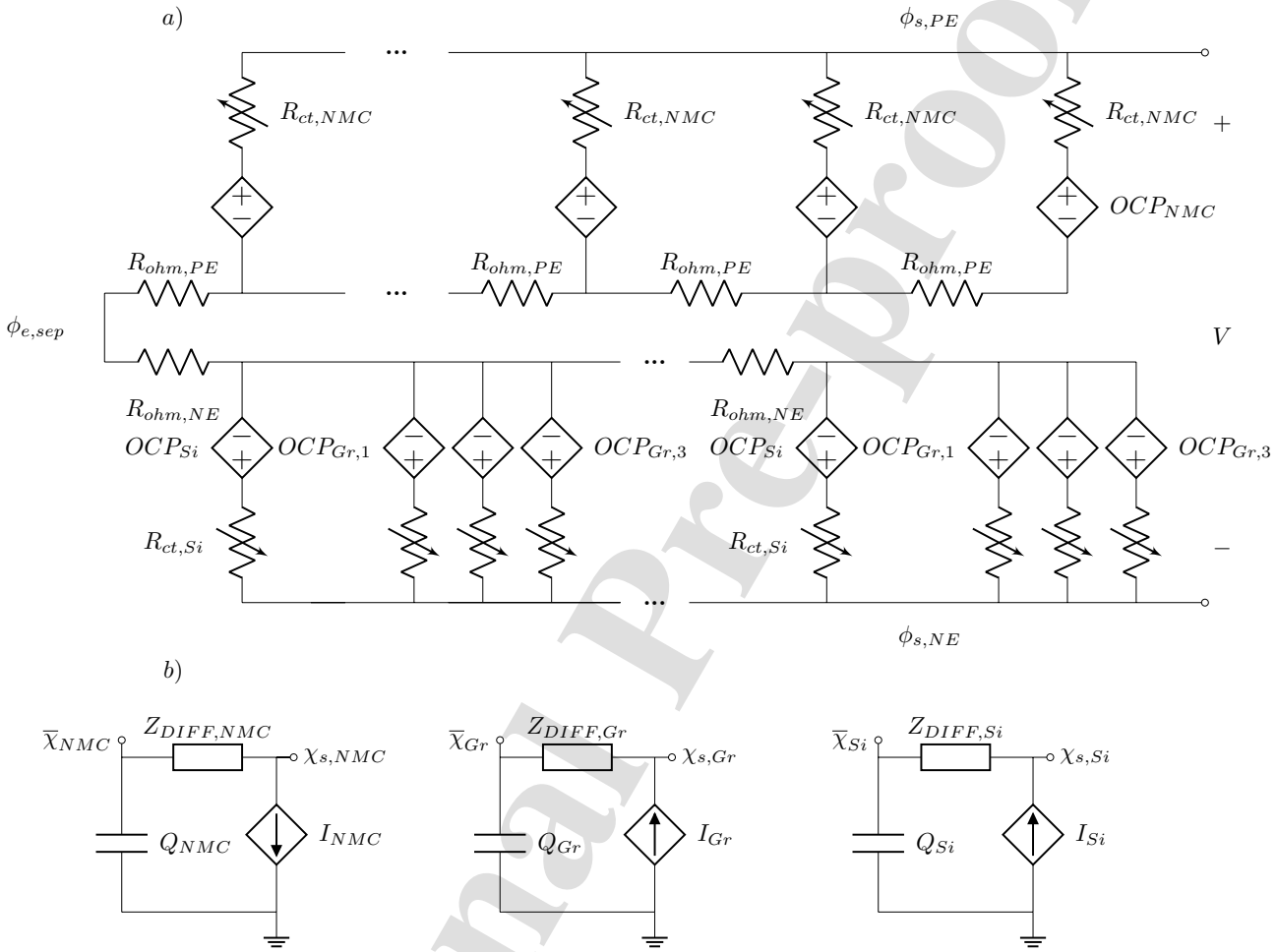

Figure 1: Discrete transmission line model for a NMC/Si-Gr cell. Subcircuit a) represents macroscale electrode structure, whereas subcircuits in b) symbolize solid diffusion in active material particles. It is noted that each controlled voltage source OCP in a) has an associated solid diffusion subcircuit like those in b), corresponding to each particle type. Z_{DIFF} stands for the impedance associated with solid diffusion after subtracting integrator dynamics. ϕ_s and ϕ_e stand for solid and electrolyte potential, whereas N_{PE} and N_{NE} indicate the number of spatial nodes in the positive and negative electrode, respectively.

3. Module simulation framework

In this section, the method for hierarchical module simulation is outlined. The 4P module in ladder configuration analyzed in this article is depicted in the schematic in Fig. 2, where R_{int} and R_{cont} denote the interconnection and contact resistances, respectively.

The simulation procedure for the ECM in Fig. 1 was outlined in our previous work and is based on the separation of timescales [64], i.e., the assumption that solid diffusion is sufficiently slower and charge transfer is sufficiently faster than the selected timestep, also made in [44]. The assumption that the charge transfer process takes place instantaneously is also made in standard formulations of the DFN model and the SPMe [65]. Ultimately, the validity of this assumption relies on the reaction kinetics of electrode materials as well as ambient temperature.

In the case of parallel-connected cells, individual cell currents are not known initially, so the circuit formulation of the model in Fig. 1 is exploited in order to derive a simplified equivalent circuit V_{eq}, R_{eq} of each cell that is substituted into the ladder structure in Fig. 2 at each timestep for the computation of the current distribution in the module. Once the current through each cell has been computed for one timestep, it is treated as the input to the cell model in Fig. 1 for the calculation of the internal current distribution within each electrode. It is noted that the values of intermediate variables V_{eq}, R_{eq} are updated at the beginning of each timestep for each cell and evolve over time with cell and module operation. As a result of the separation of timescales, the full-cell Thévenin equivalent of the TLM does not contain a transient component associated with charge transfer as it does

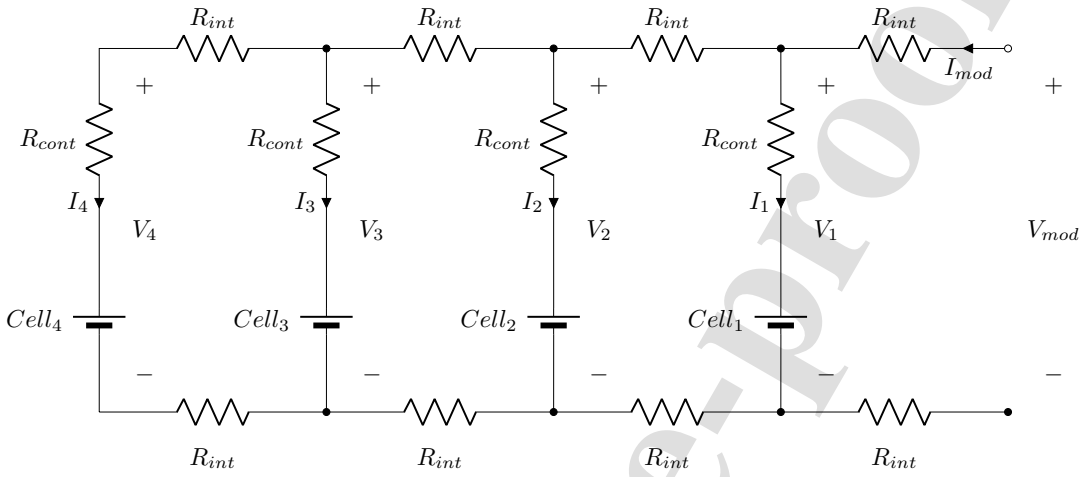

Figure 2: Schematic of the 4P module in ladder configuration, where R_{int} and R_{cont} denote the interconnection and contact resistances, respectively, and each battery symbol represents the full cell model in Fig. 1. V_{mod} and I_{mod} stand for module voltage and current, whereas $V_{1:4}$ and $I_{1:4}$ symbolize branch voltage and current, respectively.

with solid diffusion, which may lead the model to slightly overestimate the dynamic voltage response to sufficiently quick changes in current, both at cell and module levels. However, the experimental sampling time would have to be small enough to capture this transient behavior.

A detailed outline of each simulation step is provided below.

1) **Updating of solid diffusion states.** The impedance describing the dynamics of the difference between surface and average normalized concentrations in a spherical particle is defined in general as Z_{DIFF}, which is particularized for each material in Fig. 1-b). It is approximated by a series connection of three RC elements, as shown in Eq. (1).

$$Z_{DIFF}(s) = \frac{K_d}{\sqrt{\tau_d s}\coth\left(\sqrt{\tau_d s}\right) - 1} - \frac{3K_d}{\tau_d s} \approx \frac{K_d}{5}\left(\frac{a_1}{1+b_1\tau_d s} + \frac{a_2}{1+b_2\tau_d s} + \frac{a_3}{1+b_3\tau_d s}\right) \tag{1}$$

where the time constant τ_d is defined as $\tau_d = \frac{R^2}{D}$, R being particle radius and D solid diffusivity. The proportionality constant K_d is related to τ_d by the integrator constant Q which represents particle capacity $Q = \frac{\tau_d}{3K_d}$. Coefficient values a_i, b_i for the approximation are shown in Table 1 and have been determined according to the distribution of time constants associated with $Z_{DIFF}(s)$ [61].

Table 1: Coefficient values for the approximation in Eq. 1

i	1	2	3
a_i	0.5344	0.2724	0.1932
b_i	0.0479	0.0101	0.0020

Thus, the average and surface concentrations are updated according to the individual particle currents computed in the previous timestep. In order to account for the effect of solid diffusion dynamics on the current timestep, the following equivalent diffusion resistance R_{diff} is derived based on the 3RC approximation in Eq. 1 and Table 1:

$$R_{diff} = \left.\frac{\partial OCP}{\partial x}\right|_{x_s} \frac{\Delta x_s}{I} = \left.\frac{\partial OCP}{\partial x}\right|_{x_s} \cdot \left[\frac{\Delta t}{Q_p} + \sum_{i=1}^{3} \frac{K_d a_i}{5}\left(1 - \exp\left(\frac{\Delta t}{b_i \tau_d}\right)\right)\right] \tag{2}$$

where Q_p and x_s stand for particle capacity and surface concentration, respectively. This is an auxiliary resistance that is not physically

present in the model, but it is connected in series with the OCP voltage source to account for the linearized dynamic change in diffusion voltage during the current timestep. This implementation is made possible by the 3RC approximation to the solid diffusion transfer function, and provides improved numerical stability in the regions where the slope of any OCP function $\frac{\partial OCP}{\partial x}$ is large.

2) **Calculation of charge transfer resistances.** Charge transfer resistance are defined as a function of the exchange current I_0 with a nonlinear dependency on particle current I according to the Butler-Volmer equation, as shown in Eq. (3):

$$\eta_{ct} = \frac{2RT}{F}\sinh^{-1}\left(\frac{I}{2I_0}\right) \qquad R_{ct} = \frac{\eta_{ct}}{I} = \frac{RT}{FI_0}\frac{\sinh^{-1}\left(\frac{I}{2I_0}\right)}{\frac{I}{2I_0}} \tag{3}$$

The exchange current I_0 is expressed as a function of parameter K_0, which contains the temperature dependency, and its dependence on the normalized surface concentration χ_s:

$$I_0 = K_0\sqrt{\chi_s(1-\chi_s)} \tag{4}$$

The exact expression for the charge transfer resistance in Eq. (3) presents a nonlinear dependency on the ratio between particle current I and exchange current I_0. For this reason, herein the charge transfer resistances in timestep k are calculated as a function of the particle current in the previous timestep $k-1$, as shown in Eq. (5):

$$R_{ct,k} = \frac{RT}{FI_{0,k}}\frac{\sinh^{-1}\left(\frac{I_{k-1}}{2I_{0,k}}\right)}{\frac{I_{k-1}}{2I_{0,k}}} \tag{5}$$

This approach allows for an approximation to the exact value of charge transfer resistances that is more accurate than a simple linearization providing that the timestep Δt is small, and enables the computation of the equivalent resistance of each cell.

The next step for a simpler solution of the current distribution in the negative electrode is collapsing all branches n at a single node in the x dimension corresponding to silicon and different graphite particle sizes, following the approach in [31]:

$$R_{n,eq} = \frac{1}{\sum_{n=1}^{M} \frac{1}{R_{ct,n}+R_{diff,n}}}, \qquad OCP_{eq} = \frac{\sum_{n=1}^{M} \frac{OCP_n}{R_{ct,n}+R_{diff,n}}}{\sum_{n=1}^{M} \frac{1}{R_{ct,n}+R_{diff,n}}} \tag{6}$$

This is an efficient approach to the mathematical treatment of a blend of active materials as well as a particle size distribution.

3) **Calculation of full-cell Thévenin equivalents.** The distributed circuit network can be simplified by calculating its instantaneous Thévenin equivalent. For each electrode, the instantaneous Thévenin resistance R_{eq} can be computed by solving the linear system of equations in Eq. 7 with the definitions in Eq. 8. From here on, N stands for the number of spatial nodes in each electrode (N_{PE}, N_{NE}).

$$\begin{bmatrix} 1 & -1 & 0 & 0 & \dots & 0 \\ -\alpha_1 & 1+2\alpha_1 & -\alpha_1 & 0 & \dots & 0 \\ 0 & -\alpha_2 & 1+2\alpha_2 & -\alpha_2 & \ddots & \vdots \\ \vdots & 0 & \ddots & \ddots & \ddots & 0 \\ 0 & 0 & \ddots & -\alpha_{N-1} & 1+2\alpha_{N-1} & -\alpha_{N-1} \\ 0 & 0 & \dots & 0 & -\alpha_N & 1+\alpha_N \end{bmatrix} \begin{bmatrix} Z_0 \\ Z_1 \\ Z_2 \\ \vdots \\ Z_{N-1} \\ Z_N \end{bmatrix} = \begin{bmatrix} R_{ohm} \\ 0 \\ 0 \\ \vdots \\ 0 \\ 0 \end{bmatrix} \tag{7}$$

$$\alpha_{1:N} = \frac{R_{n,eq,1:N}}{R_{ohm}}, \qquad R_{eq} = Z_0 \tag{8}$$

The Thévenin voltage is calculated by solving the electrode ladder structure when the current is set to zero:

$$\begin{bmatrix} 1+\alpha_1 & -\alpha_1 & 0 & \dots & 0 \\ -\alpha_2 & 1+2\alpha_2 & -\alpha_2 & \ddots & \vdots \\ \vdots & \ddots & \ddots & \ddots & 0 \\ 0 & \ddots & -\alpha_{N-1} & 1+2\alpha_{N-1} & -\alpha_{N-1} \\ 0 & \dots & 0 & -\alpha_N & 1+\alpha_N \end{bmatrix} \begin{bmatrix} \phi_1 \\ \phi_2 \\ \vdots \\ \phi_{N-1} \\ \phi_N \end{bmatrix} = \begin{bmatrix} OCP_{eq,1} \\ OCP_{eq,2} \\ \vdots \\ OCP_{eq,N-1} \\ OCP_{eq,N} \end{bmatrix} \tag{9}$$

where $V_{eq} = \phi_1$. Finally, the full cell Thévenin equivalent is computed as the series connection of both electrodes: $R_{eq,FC} = R_{eq,PE} + R_{eq,NE}$, $V_{eq,FC} = V_{eq,PE} - V_{eq,NE}$, which is substituted into the module ladder structure for an efficient computation of the current distribution. It is emphasized that this method provides values of intermediate variables V_{eq} and R_{eq} that are electrically consistent with the dynamics of the cell model in Fig. 1 and do not depend on module-level current.

4) **Calculation of module voltage and current distribution.** For a 4P module in ladder configuration, as indicated in Fig. 2, the module voltage V_{mod} as well as the branch voltages $V_{1:N}$ can be calculated as the solution to the linear system of equations in Eq. 10 and the definition in 11.

$$\begin{bmatrix} 1 & -1 & 0 & 0 & 0 \\ -\beta_1 & 1+2\beta_1 & -\beta_1 & 0 & 0 \\ 0 & -\beta_2 & 1+2\beta_2 & -\beta_2 & 0 \\ 0 & 0 & -\beta_3 & 1+2\beta_3 & -\beta_3 \\ 0 & 0 & 0 & -\beta_4 & 1+\beta_4 \end{bmatrix} \begin{bmatrix} V_{mod} \\ V_1 \\ V_2 \\ V_3 \\ V_4 \end{bmatrix} = \begin{bmatrix} 2R_{int}I_{mod} \\ V_{eq,1} \\ V_{eq,2} \\ V_{eq,3} \\ V_{eq,4} \end{bmatrix} \tag{10}$$

$$\beta_{1:N} = \frac{R_{eq,1:N} + R_{cont}}{2R_{int}} \tag{11}$$

where $V_{eq,1:N}$ and $R_{eq,1:N}$ are the full-cell Thévenin voltages and resistances computed in the previous step, I_{mod} is the module current, R_{int} is the interconnection resistance and R_{cont} is the contact resistance. The current through each branch may be calculated from the branch voltages according to Eq. (12).

$$I_{1:N} = \frac{V_{1:N} - V_{eq,1:N}}{R_{eq,1:N} + R_{cont}} \tag{12}$$

It is possible to reiterate the procedure outlined in Step 3 to compute the instantaneous Thévenin equivalent of the module, since it is akin to the ladder structure of each electrode in the employed cell model. This enables interfacing the module with loads other than a current source. A simulation of the discharge of a module through a switched shunt resistor is provided in Fig. S4 in order to emulate the most common alternative for passive balancing.

5) **Calculation of cell electrode potential.**

Once cell currents have been computed, they are treated as the input to the ECM in Fig. 1 to calculate the potential and current distribution

within each electrode in each cell. Electrode potential is calculated as the solution to the linear system of equations in Eq. 13, characterized by cell input current, and the variables calculated in step 2.

$$\begin{bmatrix} 1 & -1 & 0 & 0 & \dots & 0 \\ -\alpha_1 & 1+2\alpha_1 & -\alpha_1 & 0 & \dots & 0 \\ 0 & -\alpha_2 & 1+2\alpha_2 & -\alpha_2 & \ddots & \vdots \\ \vdots & 0 & \ddots & \ddots & \ddots & 0 \\ 0 & 0 & \ddots & -\alpha_{N-1} & 1+2\alpha_{N-1} & -\alpha_{N-1} \\ 0 & 0 & \dots & 0 & -\alpha_N & 1+\alpha_N \end{bmatrix} \begin{bmatrix} \phi_0 \\ \phi_1 \\ \phi_2 \\ \vdots \\ \phi_{N-1} \\ \phi_N \end{bmatrix} = \begin{bmatrix} R_{ohm} I_{cell} \\ OCP_{eq,1} \\ OCP_{eq,2} \\ \vdots \\ OCP_{eq,N-1} \\ OCP_{eq,N} \end{bmatrix} \tag{13}$$

$\phi_{1:N}$ stands for electrode potential at nodes 1 through N, defined as $\phi = \phi_s - \phi_e$, and ϕ_0 is the electrolyte potential at the separator interface, measured with respect to ϕ_s. Subsequently, the current through each particle at each node may be calculated from the potential distribution in the electrode according to Eq. (14).

$$I_{1:N} = \frac{\phi_{1:N} - OCP_{eq,1:N}}{R_{n,k,1:N}} \tag{14}$$

This current will be the input to the state equation for solid diffusion for the next timestep and will also be employed to update the charge-transfer resistance for the next timestep.

The presented framework based on hierarchical model solution (electrode → cell → module → cell → electrode) proves computationally efficient, since no equations must be solved by iterative methods, while also providing insightful and interpretable information about the operation at each level. This

framework mainly consists of matrix-vector operations and tridiagonal systems of equations, which makes it suitable for its implementation in embedded systems as demonstrated for a simpler case in [66].

The equivalent circuit described by (V_{eq}, R_{eq}), with values computed according to the procedure above, is electrically consistent with the dynamics of a battery cell since it constitutes the best linear approximation to its instantaneous current-voltage relationship in the neighborhood of its current operating point. Fig. 3 qualitatively exemplifies the instantaneous current-voltage relationship of a battery cell; the curvature is due to the nonlinearity of the Butler-Volmer equation as well as the dynamics of transient processes which produce a delayed voltage response to input current.

The static resistance approach approximates the behavior at an operating point (I_0, V_0) by the static component of cell voltage OCV and the chordal resistance. However, this approach implies that the full-cell overpotential is ohmic in nature, which is not fully in accordance with the dynamics of an electrochemical model. In contrast, V_{eq} is the value of cell voltage in the theoretical low current limit for said operating point, but factoring in the current state of dynamic processes, which makes it different from the equilibrium voltage OCV. In consequence, R_{eq} enables a closer approximation to instantaneous cell dynamics around the operating point (I_0, V_0), which is required for the adequate simulation of module operation. In the case of the TLM, the Thévenin equivalent gives well-defined values of (V_{eq}, R_{eq}) regardless of the operating conditions, whereas an electrochemical model only enables the computation of the static resistance since it is not formulated in terms of circuit elements. Fig. 3 also anticipates why numerical instability

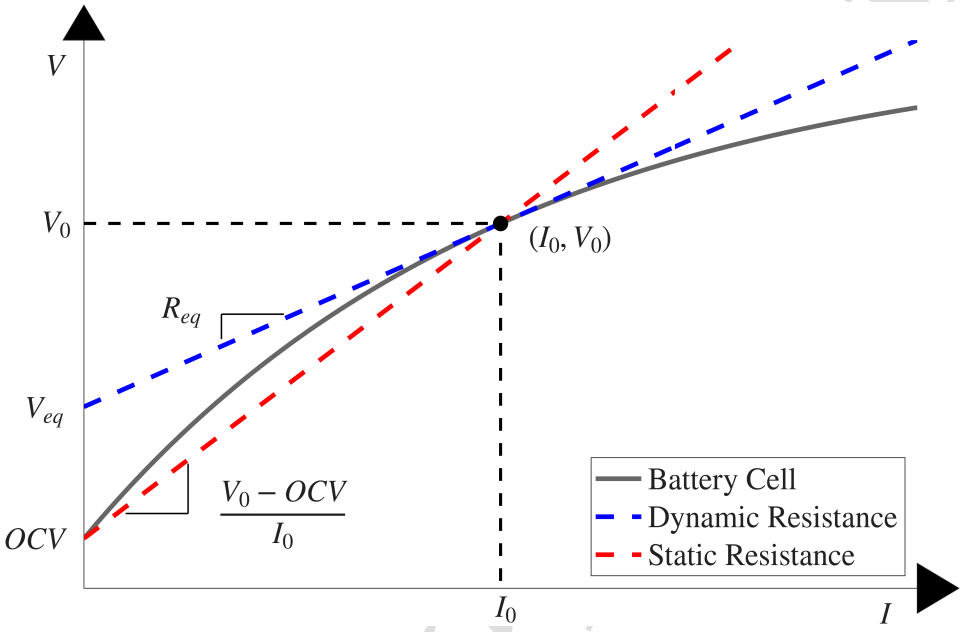

Figure 3: Schematic illustration of the difference between the static and dynamic resistance approaches for approximating the instantaneous current-voltage relationship of a battery cell at an operating point (I_0, V_0).

may arise in the calculation of the static resistance when cell current is close to zero. These aspects will be illustrated quantitatively in Section 5.3.

4. Experimental setup and testing

In this article, the dataset presented by Piombo et al. [67, 68] is employed for experimental validation. Although readers may find an extensive description of the experimental setup and equipment in the source publications [67, 68], critical details about the experimental setup and module configuration that are relevant to the research work conducted herein are re-

produced for the sake of clarity. The aforementioned experimental campaign was aimed at quantifying cell-to-cell variations in capacity and internal resistance in commercial batches, as well as analyzing the performance of a 4P module under a variety of operating scenarios considering the following input parameters: interconnection resistance, ambient temperature, chemistry, and the presence of an aged cell. In particular, the subset of experimental data corresponding to NMC/Si-Gr cells is studied in this work.

A batch of 19 commercial NMC/Si-Gr cells (INR21700-M50T manufactured by LG Chem) were analyzed. The investigated cells have a nominal voltage of 3.63 V and exhibit a nominal discharge capacity of 4.85 Ah between the voltage limits of 4.2 V and 2.5 V. Their standard constant charging current is 0.3C (1455 mA), with a maximum limit of 0.7C (3395 mA) from 25°C to 45°C. Conversely, their standard constant discharging current is 0.2C (970 mA), with maximum values of 3C (14550 mA) from 10°C to 25°C, and 1.5C (7275 mA) from 25°C to 55°C. Additionally, one identical cell from an earlier batch, stored at 50% SOC for 12 months under calendar aging conditions, was added to the pool in order to assess the effect of the presence of a slightly aged cell on module performance.

The physical configuration of the 4P module is illustrated in Fig. 4, while the magnification shows cell connections in greater detail. Hall-effect sensors (Honeywell SS495A) are employed to measure individual cell currents, while T-type thermocouples, taped to the cells' surface at mid height (not depicted in Fig. 4), are used to monitor individual cell temperatures. One additional thermocouple is employed to measure the ambient temperature inside the environmental chamber. Hall sensors are mechanically fixed to the cell holders,

measuring the current through the bolts that enable electrical contact between the cells and the busbars. The spacing between the cells is 5 mm, and both front and back sides of the cells shown in Fig. 4 are available for heat dissipation through natural convection. Two types of busbar are designed: a solid copper busbar to emulate an ideal interconnection (mounted on the module in Fig. 4), and a copper busbar composed of different segments between which precision shunt resistors are soldered (shown on the right-hand side of Fig. 4). The nominal values of the employed shunt resistors are 1 mΩ and 3 mΩ, whereas their respective average measured values are 1.05 mΩ and 3.02 mΩ. The maximum value of R_{int} (3 mΩ) was selected to be approximately 10% of the internal resistance of the investigated cell, and 1 mΩ was chosen as an intermediate value between 0 mΩ and 3 mΩ. The interconnection resistance associated with the copper busbars is calculated based on its dimensions, giving a value of 5.4 $\mu\Omega$. The value of the contact resistance (1.21 mΩ) is determined experimentally by electrically characterizing identical bolt junctions at similar levels of pressure. Module terminals are connected to the battery cycler, which provides measurements of module voltage and current.

In order to calibrate the Hall sensors, a staircase current profile with known values from -2C to 2C is tested, and the resulting voltage response is recorded, as shown in Fig. 5-a). The calibration curve for one particular sensor is shown in Fig. 5-b), including the linear fit, which enables retrieving current values from the sensor's voltage response. It is noted that Hall sensor calibration data is also available in the source dataset.

The experimental campaign comprises two separate sections: single-cell

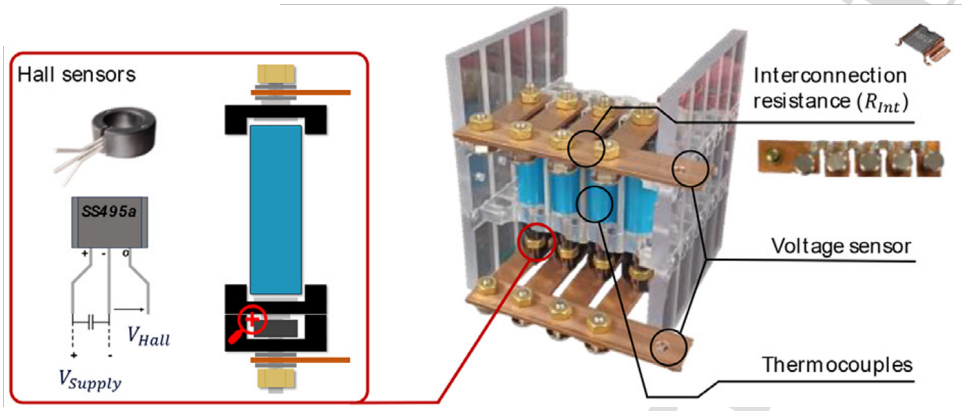

Figure 4: Physical configuration of the 4P module [67, 68].

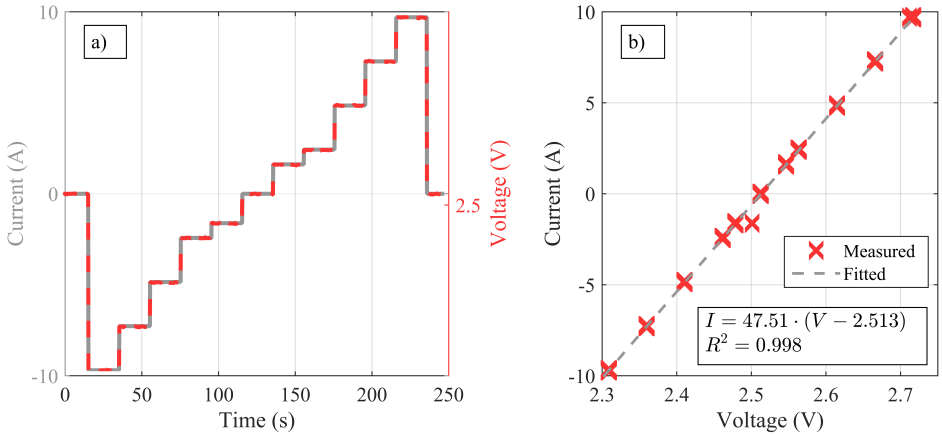

Figure 5: a) Input current (solid grey line) and Hall sensor voltage response (dashed red line). b) Linear calibration curve (dahsed grey line) and the measured voltage-current data (red crosses) for one particular Hall sensor.

characterization and module-level operation. Single-cell characterization was performed at a constant temperature of 23°C, and consisted of a pseudo-

Open Circuit Voltage (OCV) discharge at C/20 for full-cell reconstruction, and a Hybrid Pulse Power Characterization (HPPC) schedule for dynamic characterization. HPPC current pulses are applied at 10% SOC intervals from 90% SOC down to 10% SOC with a charge/discharge ratio of 0.75 (2.66 A/2 A) and a duration of 10 s. The charging procedures in this case were Constant Current-Constant Voltage (CC-CV) at C/3 up to 4.2 V, and then until a 50 mA cutoff was reached.

Module-level operation comprises a matrix of tests including 3 values of interconnection resistance (0 mΩ, 1 mΩ and 3 mΩ) and 3 ambient temperatures (10°C, 25°C and 40°C), which were then repeated for the case where the aged cell is located furthest from the module terminals (position 4 in Fig. 2), yielding a total of 18 different cases. The module-level testing protocol consisted of a CC-CV charge as described above, followed by a discharge at a nominal module rate of 0.8C (15.5 A), set so that individual cell currents are guaranteed to remain below the discharge limits specified above at all temperatures. All the experimental schedules were performed under temperature-controlled conditions, ensured by an Amerex IC500R environmental chamber, with the aid of an Arbin LBT22013 battery cycler, which is employed in conjunction with a Data Acquisition System (DAQ) in module operation for the collection of cell-level current and temperature measurements with a constant sampling time of 1 s.

5. Results and discussion

5.1. Single-cell characterization

In this section, the parameterization methodology for the TLM of a single cell in Fig. 1 is described and performed for all the cells in the batch. Based on the experimental campaigns outlined in 4, single-cell characterization is composed of two steps: thermodynamic and dynamic characterization.

1) **Thermodynamic characterization.** Pseudo-OCV discharges at C/20 are employed for the full-cell reconstruction of all 20 cells in the batch as explained below. Experimental thermodynamic profiles are shown in Fig. 6-a), whereas the full-cell reconstruction of a fresh cell is shown in Fig. 6-b). In order to ensure consistent reconstruction results, the same percentage of silicon contribution to anode capacity (11%) is assumed for all cells, as well as the initial stoichiometry values corresponding to SOC=100% ($\chi_{NMC} = 0.025$, $\chi_{Gr} = 0.93$, $\chi_{Si} = 0.99$), leaving electrode capacities Q_{PE} y Q_{NE} as the fitting parameters. Furthermore, the analytical expressions for OCPs provided in Appendix A are employed for electrode balancing, whose experimental data were originally presented in [69]. Full-cell reconstruction results are summarized by the following electrode capacities: $Q_{PE} = 5.386 \pm 0.019$ Ah y $Q_{NE} = 5.203 \pm 0.039$ Ah, with a larger variation in anode capacity and an average voltage error of 12.8 mV RMS. These results are analogous to those presented in [70] for the INR21700-M50T cell, with a minor decrease in Q_{PE} ascribed to the fact that the original half-cell data for NMC811 in [69] does not include the abrupt voltage drop at high degrees of lithiation. As a result, the estimated electrode capacity is not an absolute value,

but it is computed in relation to the available half-cell data. However, this region falls outside the full-cell operating window, and thus, it is not expected to affect full-cell simulation results. It is also noted that a slightly lower silicon contribution is obtained herein in comparison to [70] (11% vs. 15%), which is likely due to minor differences in the employed silicon OCP profile.

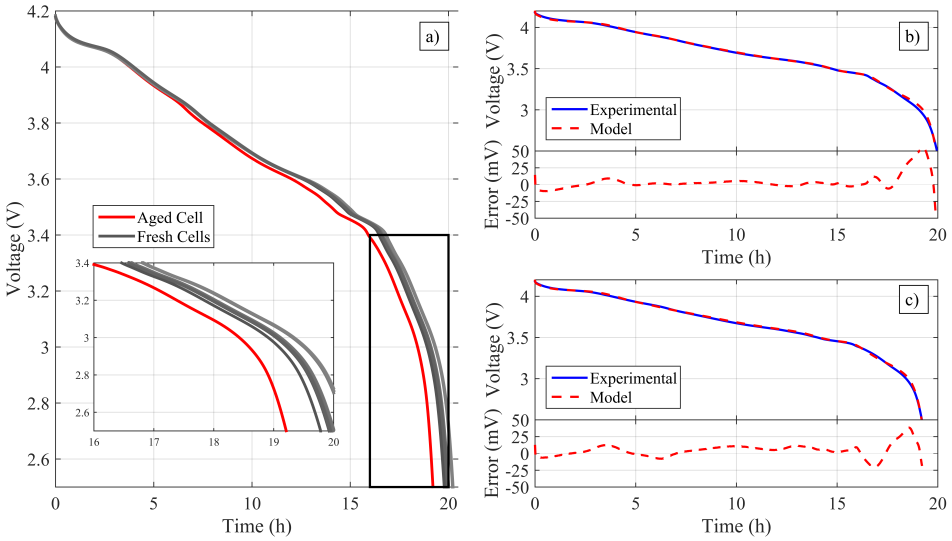

Figure 6: a) Pseudo-OCV discharge profiles at C/20 for all 20 cells in the batch. Fresh cells are plotted in grayscale, while the aged cell is plotted in red. b) Full-cell reconstruction for one fresh cell, along with voltage error between experimental and reconstructed profiles. c) Full-cell reconstruction for the aged cell, along with voltage error between experimental and reconstructed profiles.

With respect to the aged cell, full-cell reconstruction results are shown in Fig. 6-c), with a voltage error of 10.4 mV RMS. It is pointed out that, in both cases, the voltage error between experimental and recon-

structed thermodynamic profiles remains below 10 mV for SOCs above 15%, i.e., before 17 h into the C/20 discharge. A higher error is obtained in the low SOC region, where the contribution of silicon to anode capacity is the greatest, ascribed to possible differences in the behavior of silicon in full-cell and half-cell settings [69, 71]. Given that this cell was subjected to calendar aging, which is primarily associated with loss of lithium inventory, its full-cell reconstruction is performed by assuming a negative electrode shift to lower stoichiometries. However, since this cell is in only the early stages of aging (i.e., 96% of nominal capacity), there are other possibilities that are able to yield accurate full-cell reconstruction results. In any case, the goal of this analysis is to obtain an accurate OCV profile for module simulation, which is achieved, and not a comprehensive study of aging behavior. Although the TLM does not include real-time degradation submodels, it can account for the effects of degradation modes by adjusting model parameters similarly to an electrochemical model. For instance, the initial stoichiometries can be adjusted to reproduce the shift in electrode balancing due to loss of lithium inventory, whereas the capacity associated with each material can be decreased to account for loss of active material. In consequence, the TLM can effectively be reparameterized for the current state of an aged cell in order to introduce it into module simulations.

2) **Dynamic characterization.** Once the static characteristics have been determined for all cells, HPPC data is employed to determine the necessary dynamic parameters for the model in Fig. 1, i.e., solid diffusion time constants and charge transfer parameter K_0 for each

material, as well as ohmic resistances R_{ohm} for each electrode. A key advantage of the model in Fig. 1 with respect to a full electrochemical model lies in the fact that only electrical parameters are required instead of physical parameters.

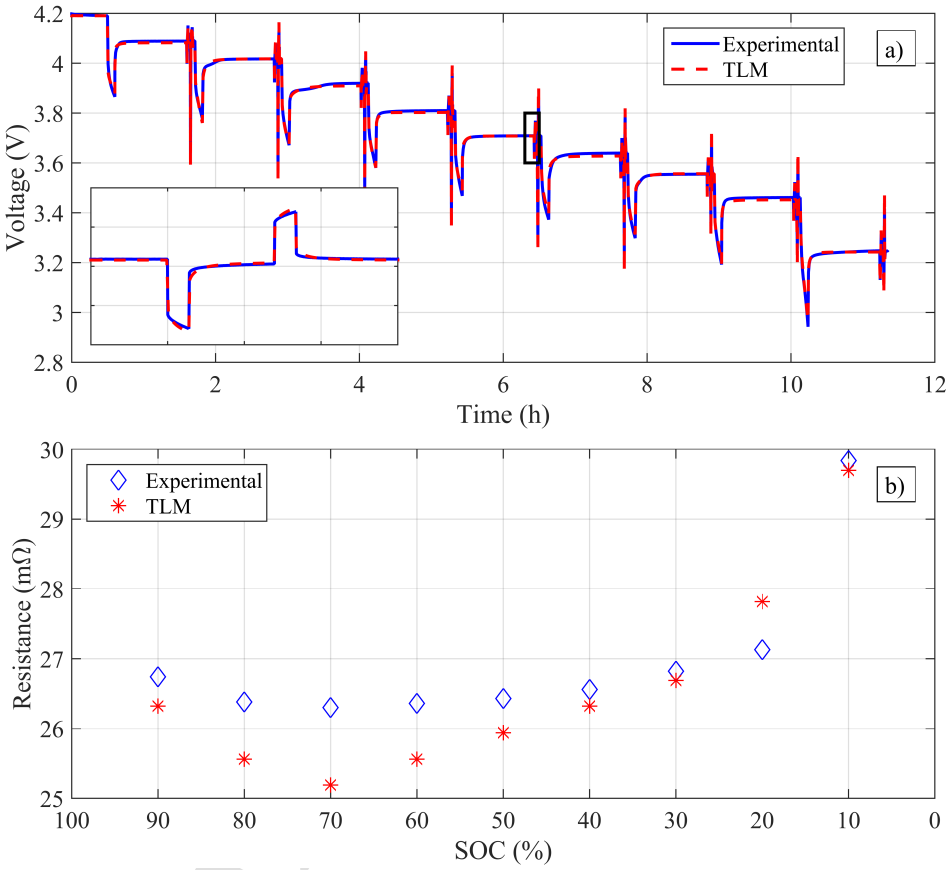

Figure 7: a) Comparison between experimental and simulated responses to the HPPC protocol for the identified model parameters. Inset depicts a detailed view of the short current pulses at 50% SOC. b) Comparison between the average HPPC resistance as a function of SOC determined experimentally and obtained from the TLM.

In our previous work [52], we detailed the parameterization methodology for the TLM for a commercial 18650 NMC811/Si-Gr cell (Samsung-SDI INR18650-35E, 3.4 Ah) also considering EIS and rate capability tests. However, the cell under study in this work is a commercial 21700 NMC811/Si-Gr cell (LG Chem INR21700-M50T 4.85 Ah). If the increase in capacity is assumed to be due to an increase in electrode area, this leads to a proportional decrease in impedance, which provides an initial parameter estimation. Although the dynamic parameters of the TLM are not completely identifiable from an HPPC profile, it is used to refine said initial parameter values with the aid of Particle Swarm Optimization. The resulting parameters are manually adjusted in order to obtain a single set of dynamic parameters valid for all cells.

A comparison between experimental and simulated responses for a sample cell is shown in Fig. 7-a); an average error of 8.98 mV RMS is obtained for the fresh cells with the parameter values reported in Table 2. A close agreement with experimental data is observed throughout the profile, including relaxation periods and equilibrium voltages, which indicate an accurate determination of diffusion time constants as well as OCV reconstruction. As shown in the inset, dynamic behavior as a response to quick current pulses is also captured, which is attributed to an appropriate description of electrode spatial structure. Fig. 7-b) shows the comparison between the average HPPC resistance determined experimentally and that obtained with the TLM for 90% SOC down to 10% SOC. It is noted that the TLM is capable of providing an accurate approximation to experimental results, with an RMS

error of 0.63 mΩ RMS (2.3%) and a maximum error of 1.11 mΩ (4.2%), which implies an appropriate description of electrode spatial structure as well as an accurate parameterization. Finally, it is noted that an accurate result (11.2 mV RMS) is also obtained for the aged cell with the same parameter set, which we ascribe to the fact that the aging on this cell is not severe enough to cause a substantial variation in dynamic behavior. It is observed that the TLM does not appear to overestimate the experimental response to the current pulses, sampled with a timestep of 0.1 s. In consequence, we hypothesize that current fluctuations down to this timescale can be simulated accurately within the range of operating conditions considered.

An additional advantage of the TLM approach in relation to conventional ECMs is the direct connection established between circuit states and internal state variables of electrochemical models beyond a current-voltage correspondence. In order to illustrate the internal behavior of the TLM, Fig. 8 shows the time evolution of internal state variables of interest that have a direct equivalence to those of electrochemical models, i.e., the normalized lithium surface concentration in NMC, silicon, and graphite active material particles and the anode potential, $\phi_{s,NE} - \phi_{e,NE}$, during the HPPC protocol shown above.

With respect to particle concentrations, it is observed that a discrete spatial distribution causes heterogeneity, with the particle located closest to the separator (Particle 1) experiencing greater fluctuations in its concentration. Regarding NMC, the greater slope of its OCP prevents large variations in concentration between particles at different spatial

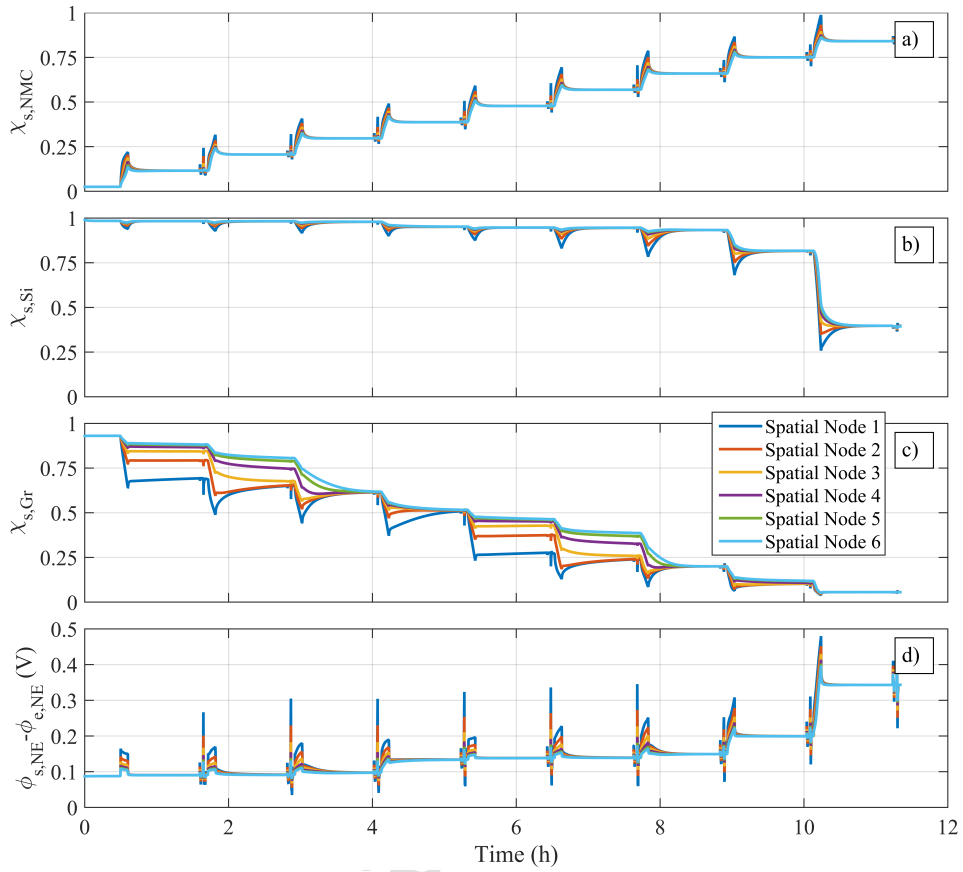

Figure 8: Time evolution of the normalized surface concentration of a) NMC, b) silicon, c) graphite active material particles, where each line corresponds to each spatial node. d) Time evolution of negative electrode potential $\phi_{s,NE} - \phi_{e,NE}$, where each line corresponds to each spatial node.

nodes, which only occur during discharge pulses. In contrast, the stepwise flat OCP profile of graphite leads to considerable heterogeneity in concentration that persists during relaxation periods, since small

voltage differences between spatial nodes translate into large variations in concentration in regions where the OCP profile is approximately flat. Another key feature of this particular cell is the blended Si-Gr anode, whose sequential operation is characterized by a predominant graphite utilization for SOCs above 20%, with silicon utilization being primarily restricted below said threshold. The spatial distribution of intercalation current within each electrode also constitutes a variable of interest; however, since it is directly correlated to concentration, it is not depicted in Fig. 8 to avoid clutter. Another relevant internal variable that may be monitored is anode potential, since a high risk of lithium plating is assumed to appear when this variable crosses the 0 V threshold. Although the behavior shown in Fig. 8 corresponds to operation under an HPPC profile, which is primarily a discharge, it is noted that the particle located closest to the separator (Particle 1) undergoes greater overpotentials both during charge and discharge pulses, therefore being at a higher risk of lithium plating as a result. For a more comprehensive discussion on behavior during charging and the onset of lithium plating for this chemistry, readers are referred to our previous work on the application of the TLM at the cell level [52]. With regard to the particle size distribution for graphite, we follow a similar approach as in our previous work [52] by defining three particle radii $\begin{bmatrix} R_1 & R_2 & R_3 \end{bmatrix} = \begin{bmatrix} 1 & 3 & 10 \end{bmatrix}$, which leads to subsequent diffusion time constants $\tau_{d,Gr} = \tau_{d,Gr,ref} \begin{bmatrix} 1 & 9 & 100 \end{bmatrix}$. The consideration of large particle sizes is because outlier particles, while not significantly increasing electrode capacity, can decisively influence the relaxation process

[72]. Additionally, although particles are generally considered to be spherical and evenly distributed, their shapes may actually be irregular, causing slower lithium redistribution [73]. Lastly, the relative capacity associated with each particle size $\begin{bmatrix}\epsilon_1 & \epsilon_2 & \dots & \epsilon_m\end{bmatrix}$ is defined and adjusted from the values in [52] to match relaxation profiles after a full module discharge. Temperature-dependent parameters τ for solid diffusion and K_0 for charge transfer are modified according to an Arrhenius equation with parameters $E_{a,dif} = 45$ kJ/mol and $E_{a,ct} = 65$ kJ/mol, in agreement with previous identification and validation results for the discrete TLM modeling approach and chemistry [52, 62]. It is noted that the Arrhenius parameters employed herein may differ from those in [59], due to the different interpretation of EIS resulting from the discrete TLM modeling approach as opposed to the traditional approach to EIS fitting based on the series connection of circuit elements [74]. A summary of parameter values is reported in Table 2.

Table 2: Dynamic model parameters

Positive electrode		**Negative electrode**			
$R_{ohm,PE}$	6 mΩ	$R_{ohm,NE}$	7 mΩ	$\begin{bmatrix}\epsilon_1 & \epsilon_2 & \epsilon_3\end{bmatrix}$	$\begin{bmatrix}0.813 & 0.163 & 0.024\end{bmatrix}$
$\tau_{d,NMC}$	4000 s	$\tau_{d,Si}$	160 s	$\tau_{d,Gr,ref}$	840 s
$K_{0,NMC}$	Very Large	$K_{0,Si}$	0.2 A	$K_{0,Gr,ref}$	1.5 A

In summary, all 20 cells in the batch, including the aged cell, are characterized thermodynamically and dynamically, resulting in specific values for electrode capacities, but uniform values for dynamic parameters. Next, each

individual cell model is introduced into the module structure for each respective case, and module operation is simulated according to the procedure described in Section 3.

5.2. Module validation

In this section, module behavior, characterized by terminal voltage and current distribution, is validated against the experimental dataset described in 4; it is worth noting that only several representative cases in the matrix of tests are shown. Although the current distribution among parallel-connected cells has been the subject of numerous previous works, herein we also emphasize the importance of simultaneously reproducing module voltage, as it determines the power and energy delivered to the load.

Simulation and experimental results are shown in Fig. 9 for the case of fresh cells at 25°C, with an interconnection resistance $R_{int} = 3$ mΩ. Regarding module voltage, it is worth noting that its magnitude and slope during the constant-current discharge are accurately matched, which we mainly ascribe to an appropriate spatial structure of the single-cell model in Fig. 1. We demonstrated in our previous work [52] that this consideration is a key aspect to reproduce cell voltage at increasing C-rates. Although the average C-rate is below 1C, individual cell currents reach peaks of 1.25C, which necessitates a cell model with a broader range of applicability. Additionally, module voltage during the relaxation phase is replicated with a high degree of accuracy, which is attributed to the incorporation of a particle size distribution for graphite. A slight voltage discrepancy is observed from t=0.8 h, reaching its maximum deviation at t=0.96 h, which is attributed to the presence of silicon; nevertheless, the overall error in module voltage is 10.0

644 mV RMS, which is indicative of the accuracy of the proposed method.

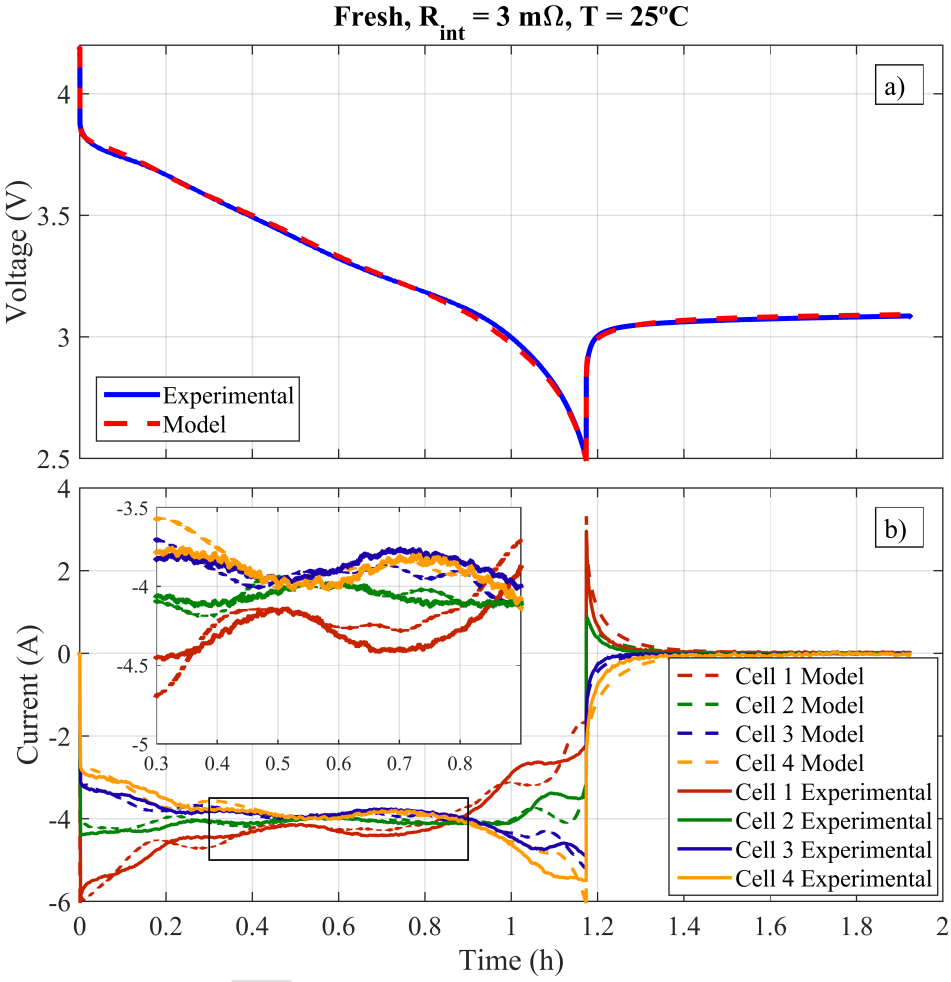

Figure 9: a) Comparison between experimental (solid) and simulated (dashed) module voltage for R_{int} = 3 mΩ and 25°C. b) Comparison between experimental (solid) and simulated (dashed) current distributions. Inset depicts a magnification on the current distributions from 0.3 h to 0.9 h.

As for the current distribution, accurate predictions are provided throughout the operating window. It is worth noting that the initial current distribution is accurately reproduced, which provides an estimation of the maximum individual cell current for this module configuration. The fluctuations in the current distribution during the middle segment of the discharge are also quantitatively replicated, as detailed in the inset of Fig. 9. Although the qualitative behavior is also similar in the final phase of the discharge, simulation results appear to be ahead of experimental results, which could be justified by the fact that the presence of silicon and the large slope of graphite in this region result in a more unstable current distribution that is more challenging to predict. In fact, the greatest current error occurs at t=1.16 h, towards the very end of the discharge. Lastly, the current distribution during relaxation is also accurately predicted, including the peak reverse balancing current, most notably on the Cell 1, which is located closest to the module terminals.

The case of an interconnection resistance $R_{int} = 1$ mΩ at 40°C is discussed next, whose results are shown in Fig. 10. With respect to module voltage, a direct consequence of a decrease in interconnection resistance is an increase in voltage throughout the constant-current discharge, also amplified by the decrease in impedance due to the higher temperature. These behaviors are captured by the model, which yields accurate predictions during both the constant-current discharge and the relaxation periods with a voltage error of 15.0 mV RMS. Regarding the current distribution, the effect of reducing the interconnection resistance is a noticeable decrease in spread, which is mostly restricted to the initial and final segments of the discharge. The model is able

to reproduce the current distribution within these regions to a high degree of accuracy (0.093 A RMS on average), as detailed in the inset of Fig. 10, as well as anticipate a faster module self-balancing as a result of the lower interconnection resistance. In this case, the largest error in both voltage and current occurs at t=1.15 h, close to the end of the discharge.

Other relevant cases where the model is validated experimentally are those in which the aged cell replaces a fresh cell in position 4 in the module. Results at 40°C with an interconnection resistance $R_{int} = 3$ mΩ are shown in Fig. 11. Similarly, the model is also capable of producing highly accurate results, matching the magnitude and slope of module voltage during discharge, as well as the profile during relaxation, with an overall voltage error of 11.1 mV RMS. Analogously, an acceptable prediction of the current distribution is provided throughout the complete process (0.137 A RMS on average), including the initial spread and the fluctuations in the middle segment, detailed in the inset. For this value of the interconnection resistance, the key difference with the case analyzed previously lies in the current distribution towards the end of the discharge: it is observed that cell 4 provides a similar current to cell 3 in this segment, which is effectively captured by the model, as with the current distribution during relaxation. In this case, the largest error in both voltage and current occurs at t=1.33 h, towards the end of the discharge.

The effect of the presence of an aged cell is also evaluated for an interconnection resistance $R_{int} = 1$ mΩ at 25°C, and results are shown in Fig. 12. In this case, a smaller value of the interconnection resistance renders cell-to-cell variations in capacity more impactful. Whereas in the previous case with $R_{int} = 1$ mΩ the current distribution was virtually uniform in the middle

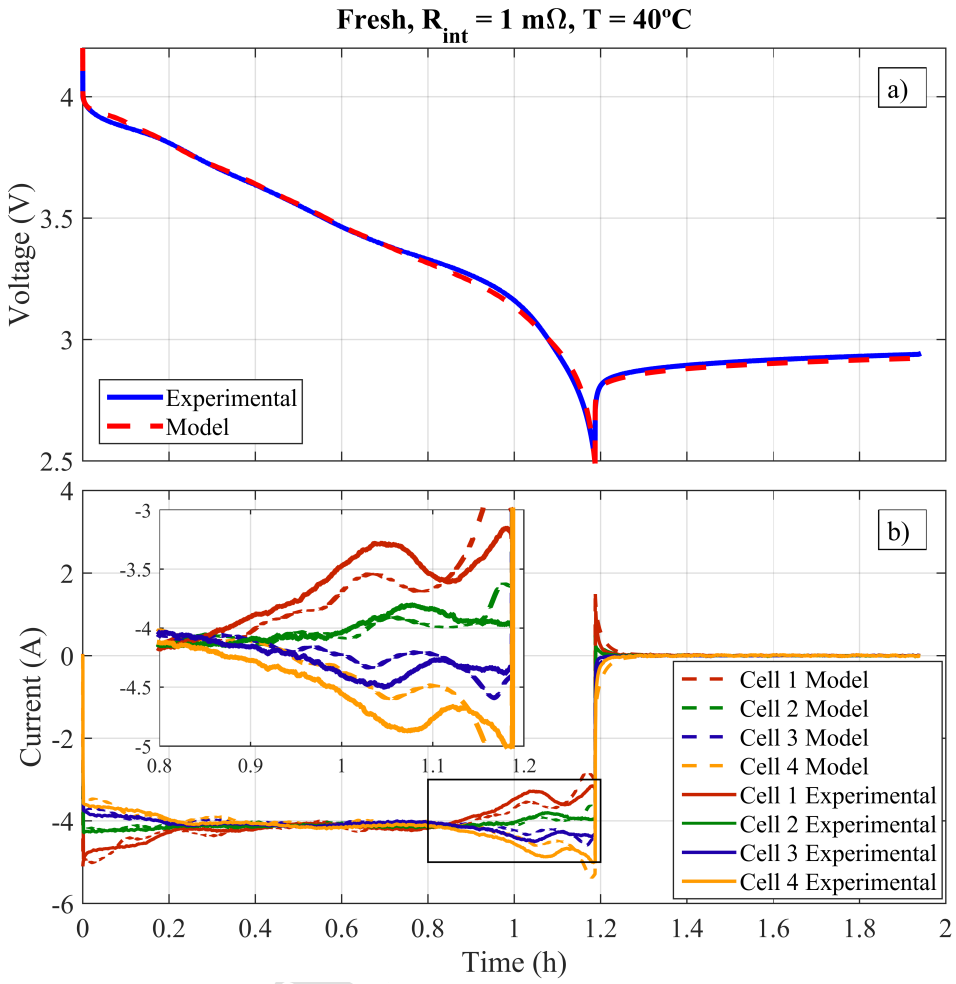

Figure 10: a) Comparison between experimental (solid) and simulated (dashed) module voltage for R_{int} = 1 mΩ and 40°C. b) Comparison between experimental (solid) and simulated (dashed) current distributions. Inset depicts a magnification on the current distributions from 0.8 h to 1.2 h.

695 segment of the discharge, the current spread in the same region increases

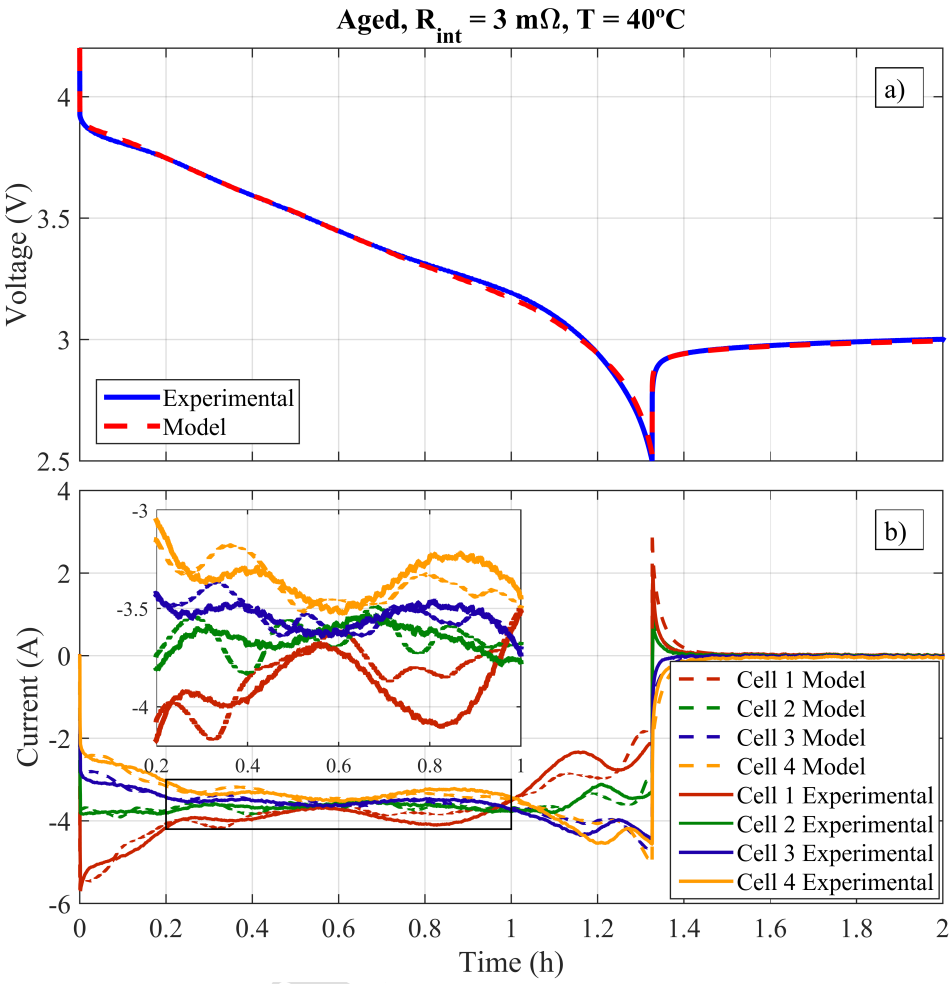

Figure 11: a) Comparison between experimental (solid) and simulated (dashed) module voltage for R_{int} = 3 mΩ and 40°C, with cell 4 being the aged cell. b) Comparison between experimental (solid) and simulated (dashed) current distributions. Inset depicts a magnification on the current distributions from 0.2 h to 1 h.

due to the presence of the aged cell in this case, with current fluctuations in cells 1 and 4. Furthermore, the cell providing the largest current towards the end of the discharge is now cell 3 instead of cell 4, which is detailed in the inset and correctly predicted by the model. In this case, the largest voltage and currents errors occur at t=1.19 h and t=1.22 h, respectively, where silicon utilization is the greatest.

Finally, the effect of the presence of an aged cell can also be studied separately by analyzing a case where R_{int} = 0 mΩ (5.4 $\mu\Omega$ in reality), as shown in Fig. 13 for 40°C. In this case, the current distribution is solely affected by cell-to-cell variations in capacity. Therefore, negligible differences are observed for the current split among the fresh cells; however, the aged cell is only able to provide a slightly lower current. This behavior is sustained throughout the discharge process, as detailed in the inset, and exacerbated in the low SOC region. The model is capable of accurately predicting the current in the aged cell, including its final uptick, as well as the fact that cell 3 counteracts this decrease in current.

A summary of model validation is presented in Table 3. Errors in module voltage and current distribution are broken down into those for just discharge and relaxation, as well as the combined case, while the value in brackets indicates the maximum error. It is worth noting that consistently accurate results are obtained for module voltage ($\leq$20mV) when considering just the discharge as well as when both discharge and the subsequent relaxation are taken into account, which is ascribed to the appropriate spatial distribution and parameterization of the employed cell model. Accurate results are also obtained for the relaxation phase, which we attribute to the consideration

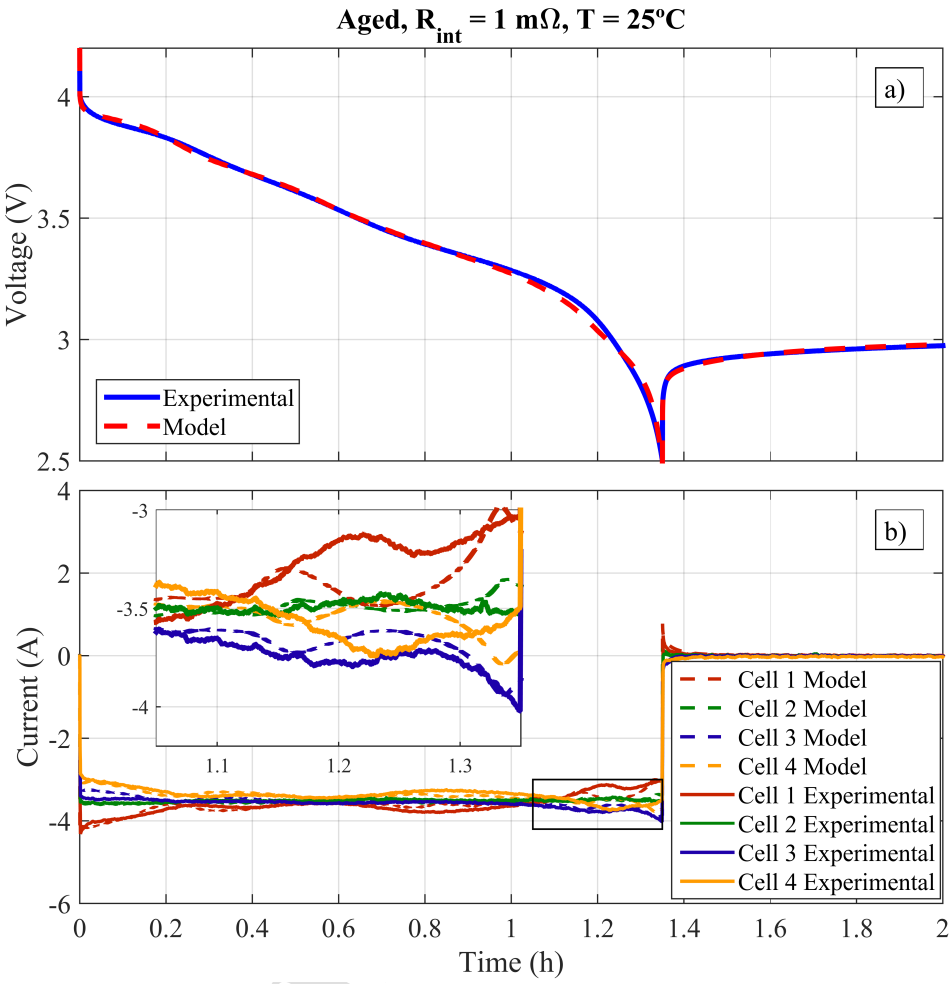

Figure 12: a) Comparison between experimental (solid) and simulated (dashed) module voltage for $R_{int} = 1m\Omega$ and 25°C, with cell 4 being the aged cell. b) Comparison between experimental (solid) and simulated (dashed) current distributions. Inset depicts a magnification on the current distributions from 1.05 h to 1.35 h.

721 of a particle size distribution for graphite. Analogously, acceptable results

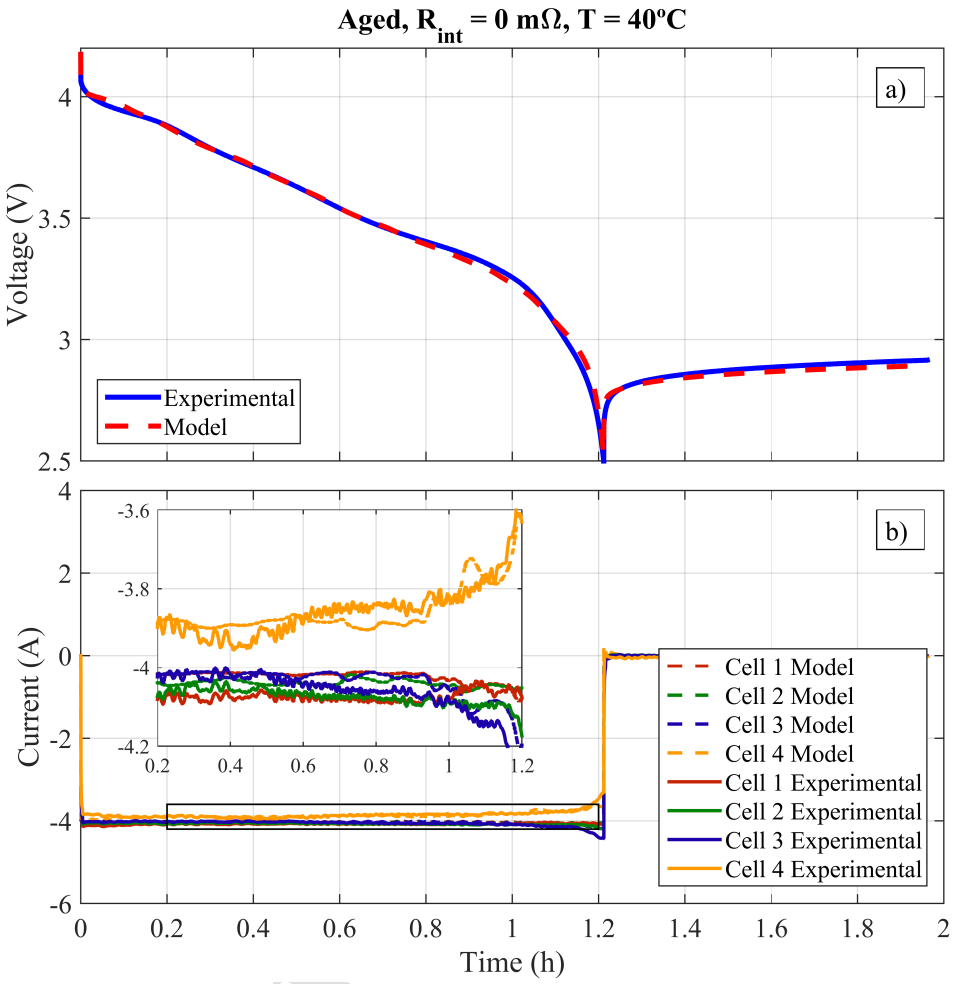

Figure 13: a) Comparison between experimental (solid) and simulated (dashed) module voltage for R_{int} = 0 mΩ and 40°C, with cell 4 being the aged cell. b) Comparison between experimental (solid) and simulated (dashed) current distributions. Inset depicts a magnification on the current distributions from 0.2 h to 1.2 h. Experimental currents have been smoothed out in order to improve visualization.

are also provided for the current distribution, although in this case, the error increases with the interconnection resistance. This is an expected outcome, since a larger interconnection resistance results in greater variability and complexity in current distribution that make it increasingly challenging to predict. It is also pointed out that the majority of the error in both voltage and current is concentrated towards the end of the discharge, due to the challenge posed by accurately modeling anode behavior in this region because of silicon utilization, the steep voltage profile of graphite, and the interactions between both materials. Given that module behavior, characterized by module voltage and current distribution, has been validated experimentally with module current as the only input, the proposed modeling framework enables obtaining information about individual cell behavior from module-level measurements. For instance, the computed current distribution may be employed to obtain an estimate of individual cell SOC and module heterogeneity.

With respect to computational cost, the presented simulation framework based on hierarchical network simplification does not require iterative numerical methods, making it computationally efficient. The average simulation time for the cases considered in Table 3, with a constant timestep $\Delta t = 0.5$, is 15.3 s per complete simulation run of approximately 2 h of real time, which equals 1.06 ms per simulation step. Nevertheless, we acknowledge that there is room for further potential improvements in numerical implementation, specifically in relation to adaptive timestepping, which lie beyond the scope of this work. A complementary discussion on numerical stability and scalability is provided in the next section.

Table 3: RMS error results for module voltage and current distribution. The value shown in brackets indicates the maximum error in the same units; the current error value is obtained as the average of the RMS values for all 4 cells. For discharge, the relative current RMS error with respect to the theoretical average current for each case is indicated in brackets. 'Aged' indicates that the aged cell has replaced a fresh cell in position 4.

		25°C			40°C		
		Discharge	Rest	Combined	Discharge	Rest	Combined
Fresh,	Voltage (mV)	17.4	10.7	15.5 (60.1)	19.4	12.6	17.1 (65.8)
$R_{int} = 0$ mΩ	Current (mA)	59.6 (1.8%)	24.0	50.8 (432.1)	75.5 (1.8%)	27.3	61.8 (316.8)
Aged,	Voltage (mV)	18.1	3.0	14.9 (75.1)	18.0	17.9	18.0 (61.2)
$R_{int} = 0$ mΩ	Current (mA)	42.3 (1.4%)	24.1	37.6 (252.3)	55.0 (1.3%)	28.8	47.2 (436.5)
Fresh,	Voltage (mV)	17.5	7.4	14.7 (47.5)	15.3	14.6	15.0 (37.8)
$R_{int} = 1$ mΩ	Current (mA)	92.6 (2.6%)	37.3	77.3 (448.2)	110.5 (2.7%)	50.8	92.2 (484.4)
Aged,	Voltage (mV)	16.4	5.1	13.6 (45.3)	17.0	17.0	17.0 (46.0)
$R_{int} = 1$ mΩ	Current (mA)	83.3 (2.4%)	27.8	69.3 (401.4)	107.4 (2.6%)	45.9	88.9 (620.3)
Fresh,	Voltage (mV)	11.6	6.7	10.0 (27.0)	13.6	10.1	12.5 (49.1)
$R_{int} = 3$ mΩ	Current (mA)	179.8 (4.4%)	93.9	153.1 (765.1)	129.1 (4.0%)	85.3	116.7 (752.2)
Aged,	Voltage (mV)	13.2	3.5	10.5 (32.0)	13.2	5.5	11.1 (38.3)
$R_{int} = 3$ mΩ	Current (mA)	171.6 (4.4%)	94.5	147.1 (712.9)	155.5 (4.3%)	94.6	136.8 (794.7)

The module simulation framework presented herein does not include a thermal submodel; however, in the cases shown above at 25°C and 40°C ambient temperatures, cell temperature increase is not large enough to considerably alter cell behavior. For instance, the average temperature increase throughout the discharge is below 2°C, and the maximum temperature increase is below 4°C and only occurs at the very end of the discharge for some cells. Furthermore, thermal interaction between cell is not expected to be significant in these cases due to cell spacing. Nevertheless, this assumption leads to inaccuracies in scenarios where cell temperature increase is significant and effectively modifies cell impedance, such as low ambient temperatures or high currents, which in turn affects the current distribution. For example, we have verified that the development of an accurate model at 10°C ambient temperature requires a coupled electrothermal model; however, the main challenge in this case lies in an accurate characterization of thermal boundary conditions, which may be different for each cell, as well as inter-cell thermal interactions. Therefore, the development of a coupled electrothermal model of a parallel module, including the computation of heat generation at the cell level as well as the thermal interaction between cells, constitutes the subject of further research, for which the proposed framework may serve as a starting point.

5.3. Analysis and discussion

Once the proposed modeling framework has been validated experimentally, the effect of the interconnection resistance R_{int} on the current distribution and module voltage is studied through simulation without the impact of real-world cell-to-cell variations, by employing the average electrode capacity

for each cell for increasing values of R_{int}. A comparison is also established with the behavior of the equivalent lumped cell, i.e., a model with electrode capacity values four times larger and impedance parameter values four times smaller. Simulation results for module voltage and current spread (maximum and minimum individual cell current values at each instant) for a 4P module are shown in Fig. 14 for $R_{int} = 0$ mΩ to $R_{int} = 5$ mΩ.

Regarding module voltage, it is observed that the lumped cell approximation is only accurate in the ideal case where the interconnection resistance is precisely 0 mΩ; a noticeable drop in module voltage is observed even when $R_{int} = 1$ mΩ, which is a realistic value [17]. The effect of the interconnection resistance is a more pronounced decrease in module voltage than in discharge capacity. In fact, an incremental voltage drop of approximately 72 mV on average for every 1 mΩ increase in R_{int} is observed, which translates into an incremental 1.4 W decrease in delivered power. The current distribution shows the characteristic behavior observed in previous experimental results, with an initial current spread due to the current step and the nonlinear shape of the OCV in the high SOC region. As the OCV-SOC relationship becomes approximately linear, the current distribution becomes increasingly homogeneous; the steep slope of the OCV at low SOCs causes further heterogeneity in the current distribution. The magnitude of the current spread is determined by the factor β, with larger values of R_{int} resulting in greater heterogeneity. It is observed that, while the nominal module current is 1C, discharge peaks ranging from 1.2C to 1.8C are reached during the initial segment of the discharge due to the effect of R_{int}. A key consequence of this is that module current has to be derated to ensure that no individual cell

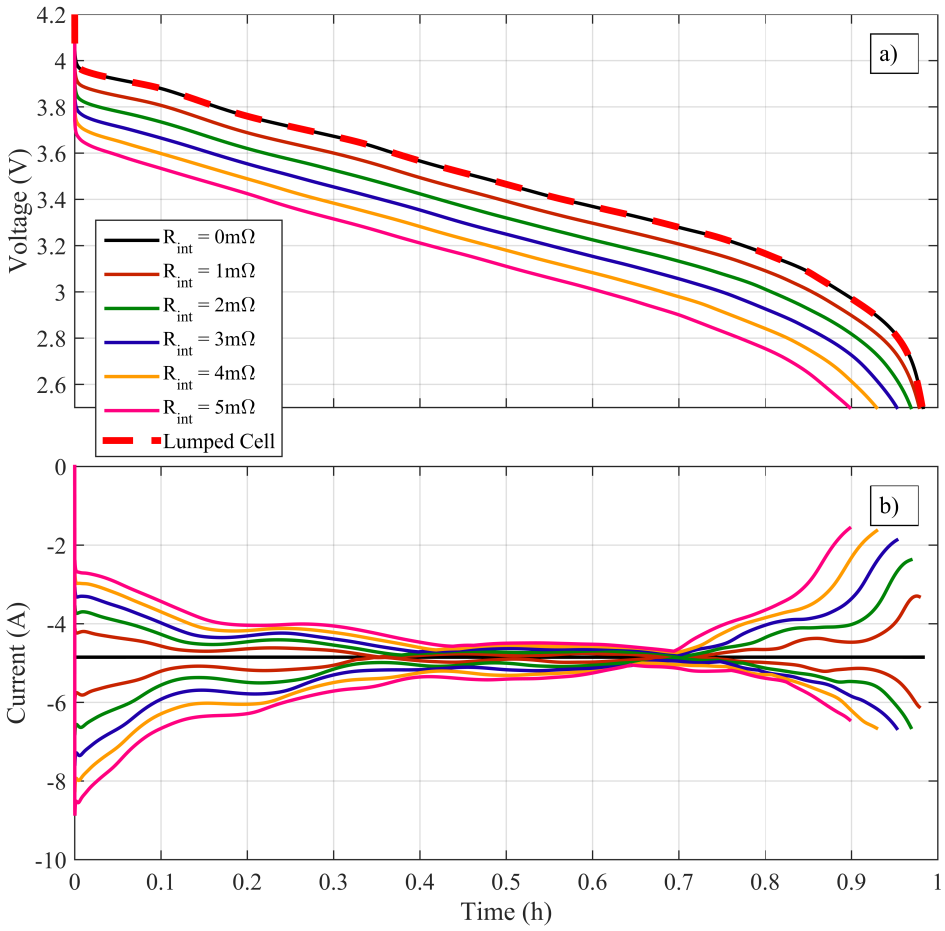

Figure 14: a) Comparison between simulated module voltage for a nominal 1C discharge for $R_{int} = 0$ mΩ to $R_{int} = 5$ mΩ for a 4P module. The behavior of the lumped cell is plotted in dashed lines. b) Simulated current spread (maximum and minimum individual cell current values at each instant) for a nominal 1C discharge for $R_{int} = 0$ mΩ up to $R_{int} = 5$ mΩ for a 4P module

exceeds its respective current limit. Given the complex behavior exhibited by the current distribution, a further extension of the present work consists of the development of dynamic derating strategies [75] and the estimation of power limits [43] as a function of the instantaneous current distribution. Furthermore, the presence of a nonzero interconnection resistance slightly increases observability, and makes module behavior sensitive to cell arrangement. For this reason, the observability analysis of the module based on the presented modeling framework constitutes the basis of further research.

In order to highlight the differences between the presented framework and established alternatives for module simulation based on electrochemical models, a comparison is made against `liionpack` [50], as well as the integration of PyBaMM [51] and Simulink. `liionpack` uses PyBaMM models for the simulation at the cell level, which are replaced by an equivalent circuit, composed of a voltage source and a series resistance, for the computation of the current distribution at the module level following the static resistance approach detailed in Fig. 3. At the time of writing, `liionpack` only allows simulations with the SPM or SPMe at the cell level, and thus, module simulations employing more comprehensive cell models, such as the DFN or DFN Si/Gr, are not possible. In order to circumvent this issue, we also follow the approach outlined in [76] to integrate PyBaMM with Simulink. In this case, Simulink handles module-level operation, and calls a PyBaMM object that steps the electrochemical model forward. The interfacing between the PyBaMM model and Simulink is also done via an equivalent circuit following the same approach as in `liionpack`.

The performance of the proposed framework is compared to that of `liionpack`

with the SPM and SPMe, as well as the integration of PyBaMM and Simulink with the SPM, SPMe, DFN and DFN Si/Gr models for the case of fresh cells at 25°C with $R_{int} = 3$ mΩ and a timestep $\Delta t = 1$ s, equal to the experimental sampling time. In order to recalibrate the parameter set in [59] for the particular cell tested in this work, we follow a similar approach to that employed by Fasolato et al. [45] for the same purpose, by adjusting active material volume fractions and leaving dynamic parameters unchanged. The suitability of this approach is verified by validating the same HPPC protocol, with results shown in Fig. S2; we understand that a thorough reparameterization of electrochemical models is beyond the scope of this paper. A more detailed account of the configuration of PyBaMM models is provided in Appendix B.

Experimental data for the case of fresh cells at 25°C with $R_{int} = 3$ mΩ are compared to simulation results with the TLM and `liionapack` with the SPMe in Fig. 15; we have verified that simulations with the DFN give very similar outcomes with respect to the SPMe for this parameter set, so its respective results are not plotted to avoid clutter. Regarding module voltage, it is noted that the SPMe is capable of providing reasonably accurate results during the CC phase (34.6 mV RMS vs. 11.6 mV RMS for the TLM); however, the SPMe is not able to match the magnitude and slope of module voltage from t=0.6 h to t=1 h, which we mainly ascribe to the lack of an appropriate spatial structure of the electrodes. Furthermore, the module voltage given by the SPMe shows an excessively abrupt voltage drop towards the end of the discharge, which is attributed to the absence of a separate silicon phase in this model. As for the current distribution, the SPMe is also able to provide reasonably accurate results in terms of RMS current error

(5.2% vs. 4.4% for the TLM); however, it is noted that the TLM is capable of following the experimental profiles more closely, particularly between t=0.4 h and t=1 h, with fewer and less pronounced fluctuations. This is mainly ascribed to the spatial distribution of the electrodes in the TLM that is not present in the SPMe, which smooths out cell voltage and results in a more stable current distribution. We acknowledge that SPMe parameters may be further optimized for this particular cell; however, we believe that the differences pointed out are qualitative and not fully explainable by variations in parameter values.

In order to showcase the differences in simulation methodology, the intermediate variables V_{eq}, R_{eq} of each cell are plotted in Fig. 16 for the previous case. Fig. 16 constitutes a quantitative illustration of the behavior described in Fig. 3: during discharge, the value of OCV is higher than that of V_{eq}, which in turn leads to higher resistance values for `liionpack` with respect to the TLM. This is a direct consequence of how V_{eq} is computed in both cases: in `liionpack`, V_{eq} is just the difference of the OCPs evaluated at surface concentrations, whereas in the TLM V_{eq} is determined by the potential distribution along the electrodes, which contains contributions from ionic transport and charge transfer beyond just the OCP values. Crucially, the equivalent resistances given by the TLM during discharge are consistent with the experimental HPPC resistance values in Fig. 7, whereas those given by `liionpack` slightly overestimate their respective HPPC values shown in Fig. S2. This highlights the improved consistency between cell and module behaviors enabled by the TLM.

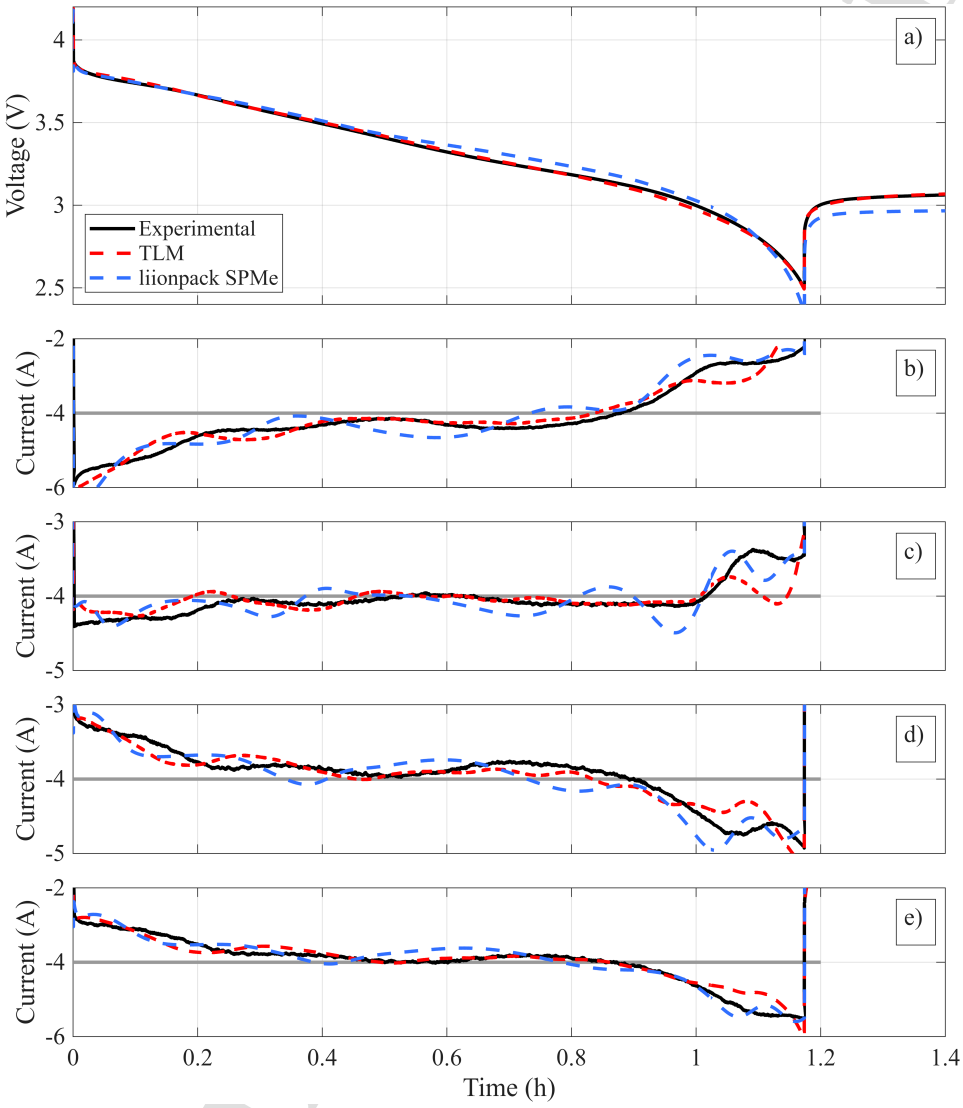

Figure 15: Comparison between experimental results (solid black) and simulation results obtained with the TLM (dashed red) and liionpack with the SPMe (dashed blue) for the case of $R_{int} = 3$ mΩ and T = 25°C. a) shows module voltage, and b) - e) show individual cell currents during discharge. The horizontal gray line in b) - e) indicates the average cell current during discharge.

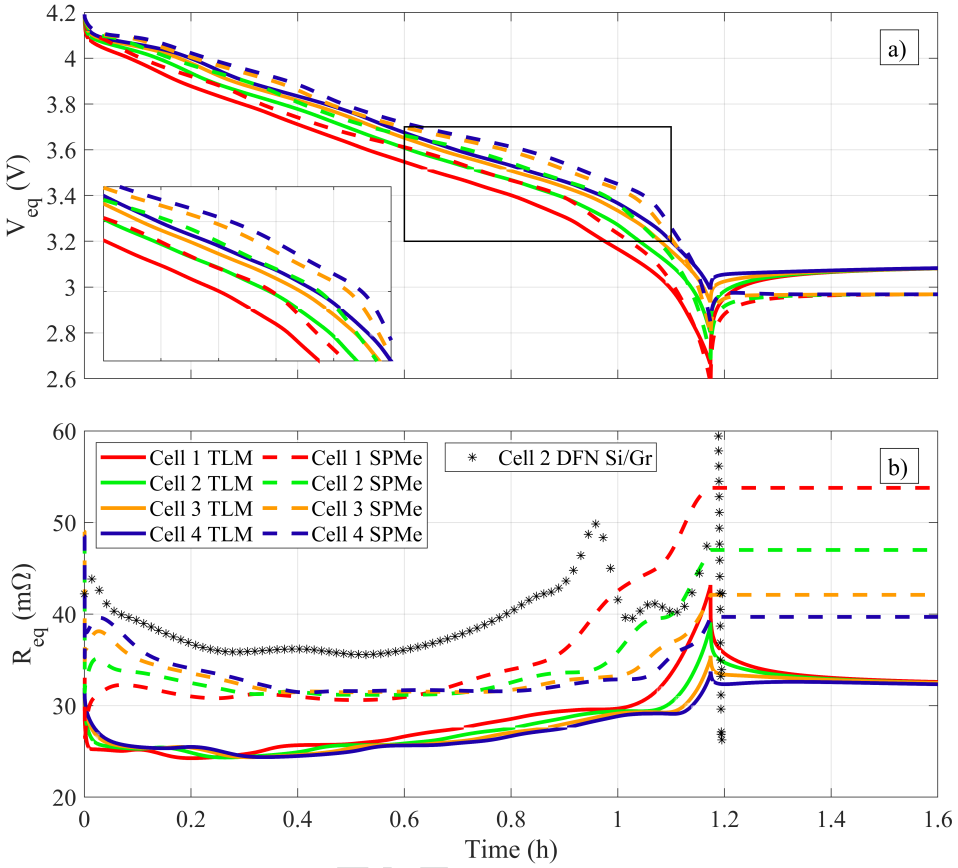

Figure 16: Comparison between the intermediate variables a) V_{eq} b) R_{eq} for all 4 cells given by the TLM (solid) and the SPMe with `liionpack` (dashed), with the same color for each cell. The inset in a) shows the equivalent voltages between t=0.6 h and t=1.1 h. Additionally, b) shows the time evolution of R_{eq} one exemplary cell for the DFN Si/Gr model (black asterisks), where the numerical divergence at t=1.2 h is observed.

Furthermore, `liionpack` does not update the calculation of R_{eq} during module relaxation to avoid numerical instability; however, this results in constant values of R_{eq} with a substantial spread between cells in a period where

they should converge towards the same value due to SOC equalization, as shown by the TLM in Fig. 16-b). The black asterisks show an example of the evolution of R_{eq} obtained with the DFN Si/Gr model with the PyBaMM/Simulink integration. In this case, R_{eq} is always computed as the static resistance, which leads to numerical instability when cell current is sufficiently close to zero or opposite sign to cell overpotential as is the case during module relaxation, and eventually results in convergence failure at t=1.2 h. In summary, the formulation of electrochemical models does not enable a simple integration into module simulations and requires approximations for the calculation of V_{eq} and R_{eq}, which can lead to inconsistency and numerical instability. Conversely, these issues are not present in the TLM-based approach since V_{eq} and R_{eq} are intrinsic properties of the model that only depend on its current state, and can be computed independently regardless of the operating conditions.

Table 4 compares the computational requirements for the considered approaches for the same simulation case. The TLM enables a more computationally efficient simulation, on the order of 4 times faster than the SPMe and over an order of magnitude quicker than the DFN and DFN Si/Gr models, while including a spatial distribution as well as separate silicon and graphite phases as the latter. The standard PyBaMM discretization consists of 20 points within each particle, and 20 points in each domain, which leads to the respective number of states for a 4P module indicated Table 4. In contrast, the approximation to solid diffusion dynamics in Eq. 1 only requires 4 states per particle, which implies 24 states per electrode and 192 for a 4P module for the TLM. A separate silicon phase entails 24 additional states per cell,

producing a total of 288 states, and two additional particle sizes for graphite increase the total count to 480 states. It is noted that the number of states for the TLM is the same order of magnitude as the SPM and SPMe while providing a physical description closer to that of the DFN Si/Gr.

Table 4: Comparison between computational requirements for the case of a 4P module at 25°C with $R_{int} = 3$ mΩ; all simulations are conducted on an Intel Core i9-10900K processor at 3.70 GHz with 128 GB of RAM. The asterisk (*) indicates that this simulation failed to converge during relaxation, therefore the corresponding value is only for the simulation time up until that point.

	Time (s)	Number of states
TLM ($\Delta t = 0.5$ s)	14.3	480 (288/192)
`liionpack` SPM ($\Delta t = 1$ s)	56.7	160
`PyBaMM/Simulink` SPM ($\Delta t = 1$ s)	57.4	160
`liionpack` SPMe ($\Delta t = 1$ s)	60.2	240
`PyBaMM/Simulink` SPMe ($\Delta t = 1$ s)	69.5	240
`PyBaMM/Simulink` DFN ($\Delta t = 1$ s)	302.7	3440
`PyBaMM/Simulink` DFN Si/Gr ($\Delta t = 1$ s)	270.2*	5040

The scalability of the proposed approach is assessed in comparison to `liionpack` with the SPMe and a timestep $\Delta t = 1$ s with an increasing number of cells connected in parallel. For the TLM, the timestep and number of cells are varied until numerical instability is encountered, and respective results are summarized in Table 5. It is pointed out that the TLM-based approach outperforms `liionpack` for smaller modules, and provides comparable performance for larger modules. For instance, a value of 1 ms per

simulation step is obtained with the TLM for a 4P module with $\Delta t = 0.5$ s, whereas this value is 8 ms per simulation step with `liionpack` for the same case. Furthermore, the TLM-based approach scales linearly, with an average increase of 2.27 s per additional cell, while `liionpack` scales slightly superlinearly, with an average increase of 1.39 s per additional cell. However, the larger increase of computation time per cell can be justified by the effects included in the TLM that are not present in the SPMe. It is also noted that the simulation times in Table 5 are contingent on numerical implementation and timestepping; therefore, we leave open the possibility of a more sophisticated implementation that further increases the computational efficiency of the TLM-based approach.

Table 5: Simulation times in seconds for `liionpack` with the SPMe and the TLM-based approach for an increasing number of cells connected in parallel. The dash (-) indicates the cases where numerical instability is encountered for the TLM. All simulations are conducted on an Intel Core i9-10900K processor at 3.70 GHz with 128 GB of RAM.

	4P	8P	12P	16P	20P	24P	28P	32P
`liionpack` (SPMe, $\Delta t = 1$ s)	28.97	33.54	38.40	43.57	49.00	54.75	60.98	67.72
TLM ($\Delta t = 0.6$ s)	6.23	12.28	-	-	-	-	-	-
TLM ($\Delta t = 0.5$ s)	7.48	14.74	22.24	29.46	-	-	-	-
TLM ($\Delta t = 0.4$ s)	9.32	18.36	27.70	36.73	45.83	55.05	63.90	72.90

Lastly, lumped ECMs are a common alternative for the simulation of parallel-connected cells. For this reason, we include a final comparison between the TLM and the 2RC ECM regarding module voltage and current distribution for the case of $R_{int} = 1$ mΩ at 25°C, in order to illustrate the differences in the module operation given by lumped and distributed ECMs.

In order to characterize the 2RC ECM, the OCV-SOC relationship and cell capacities are taken from respective thermodynamic tests, and dynamic parameters are adjusted according to the HPPC test carried out at 25°C. A key drawback of standard ECMs is that they require empirical dependencies of parameters with SOC, shown in Fig S3, which are implemented via interpolation between values determined experimentally at each SOC.

Results are shown in Fig. 17. Regarding module voltage, the 2RC ECM is able to provide reasonably accurate results for a considerable portion of the discharge, but yields large errors at low SOCs, resulting in an error of 35.6 mV RMS for the CC phase vs. 11.6 mV RMS for the TLM. However, the most interesting difference in behavior is observed in the current distribution. A spatially distributed cell model results in a smoother voltage response, which in turn leads to a more stable current distribution. Conversely, in a lumped cell model, the voltage profile is directly dictated by the shape of the OCV. Consequently, the 2RC ECM is capable of providing accurate results for the current distribution in the SOC regions where the OCV is approximately linear. Nevertheless, when a cell enters a SOC region where the OCV is nonlinear, fluctuations in the current distribution are induced to balance module voltage, which are mainly observed in the low SOC region. This highlights the importance of an appropriate spatial distribution at the cell level, and indicates that lumped ECMs may give less accurate predictions of the current distribution for chemistries where the nonlinearities of the OCV are more pronounced.

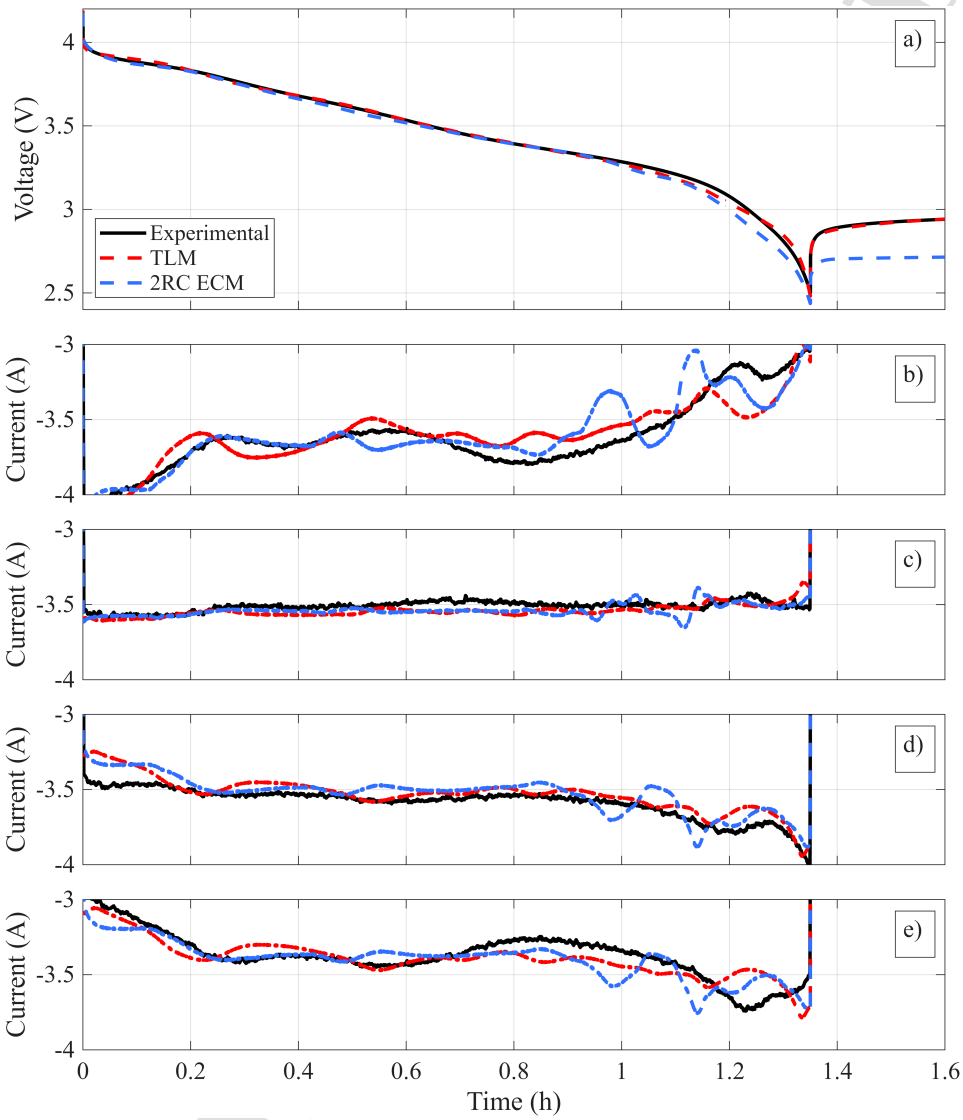

Figure 17: Comparison between experimental results (solid black) and simulation results obtained with the TLM (dashed red) and the 2RC ECM (dashed blue) for the case of R_{int} = 1 mΩ and T = 25°C. a) shows module voltage, and b) - e) show individual cell currents during discharge. The horizontal gray line in b) - e) indicates the average cell current during discharge.

In any case, the current distribution obtained with the 2RC during discharge exhibits comparable accuracy (2.5% vs. 2.4% for the TLM), which underscores the importance of a simultaneous validation of both module voltage and current distribution, as the constraint imposed by the total module current may mask the inaccuracies in the description of cell dynamics. Finally, although the 2RC ECM is lightweight, its computational efficiency is dependent on the procedure through which the OCV and dynamic parameters are interpolated for each SOC.

6. Conclusions

In this article, a method for the consistent calculation of the equivalent voltage and resistance of a battery cell is presented according to the physically motivated discrete transmission line model, which enables the efficient simulation of a module composed of cells connected in parallel. The proposed modeling and simulation methodology is validated experimentally against a dataset of a 4P module with the interconnection resistance, ambient temperature, and the presence of an aged cell as input parameters, with accurate results for module voltage ($\leq$20 mV RMS) and current distribution ($\leq$4.4% RMS). The interconnection resistance is identified as a key factor, with even small values leading to a significant drop in module voltage and an increasingly heterogeneous current distribution.

The presented methodology is compared to established approaches for the physically motivated simulation of battery modules. The consistency between module-level behavior and cell-level dynamics enabled by the proposed framework is emphasized, as well as its improved computational efficiency.

The key differences between the module behaviors given by lumped and distributed ECMs are shown to be a more accurate description of module voltage and a more stable current distribution in the latter case.

In conclusion, we understand that the proposed approach based on the transmission line model and hierarchical simplification constitutes a suitable methodology for the physically motivated simulation of parallel-connected cells, thus overcoming the challenging integration of electrochemical models into module simulations.

Acknowledgments

This work was partially supported by the Spanish Ministry of Science and Innovation via Project PID2023-151251OB-I00, by the Vice-Rectorate for Research and Knowledge Transfer at the University of Granada via Applied Research Project C-ING-188-UGR23. Pablo Rodríguez-Iturriaga acknowledges grant FPU22/00501 by the Spanish Ministry of Science and Innovation. Simona Onori would like to thank the Bits and Watts Initiative within the Precourt Institute for Energy at Stanford University for its partial financial support.

Appendix A. Open Circuit Potentials for the TLM

$$\begin{aligned} OCP_{NMC}(x) = 3.501 + 0.36 \cdot (1 + \exp\left[4.1x\right] \cdot (0.067948x - 0.0845206)) + \\ 0.0208 \cdot (1 - \exp\left[46x - 46\right]) + \frac{0.030}{1 + \exp\left[41x - 34.194\right]} + \\ \frac{0.194}{1 + \exp\left[14x - 6.062\right]} + \frac{0.113}{1 + \exp\left[42x - 9.156\right]} + \frac{0.43}{1 + \exp\left[46x + 0.138\right]} \end{aligned} \quad \text{(A.1)}$$

$$OCP_{Gr,delith}(x) = 0.06 + 0.0305 \cdot (1 - \exp[34x - 34]) + \frac{0.048}{1 + \exp[39x - 22.234]} + \frac{0.075}{1 + \exp[55x - 9.24]} - \frac{0.02}{1 + \exp[55x - 6.6]} + \frac{0.254}{1 + \exp[102x - 5.916]} + \frac{0.163}{1 + \exp[130x - 3.77]} + \frac{0.83}{1 + \exp[120x - 0.444]} \quad \text{(A.2)}$$

$$OCP_{Si,delith}(x) = 0.022 + 0.010 \log[-100x + 100.01] - 0.069 \log[0.996016x + 0.0398406] + 0.033 \cdot (1 - \exp[1650x - 1650]) \cdot (-4300x + 4301) + 0.088 \cdot (1 - \exp[21x - 21]) + \frac{0.099}{1 + \exp[12x - 8.1]} + \frac{0.0084}{1 + \exp[25x - 6.25]} + \frac{0.20}{1 + \exp[66x - 0.594]} \quad \text{(A.3)}$$

Appendix B. Notes on the configuration of PyBaMM models

The PyBaMM models integrated into Simulink are from PyBaMM 22.8. For the DFN and DFN Si/Gr models, the format of the Simulink object provided in [76] is modified to match that of the PyBaMM integrator. For the DFN model, V_{eq} is computed as the difference between the electrode-averaged values of the OCPs. For the DFN Si/Gr model, the equivalent voltage of the negative electrode is computed by means of a weighted average of the OCPs of both materials according to their relative contribution to anode capacity. We acknowledge that this is an arbitrary choice; however, there is no workaround for this issue since there are two distinct values for the electrode-averaged surface OCP. Finally, silicon hysteresis has been manually disabled for the DFN Si/Gr model by only making use of the silicon delithiation OCP, otherwise numerical convergence at the module level is severely hindered.

References

[1] W. Chen, J. Liang, Z. Yang, G. Li, A review of lithium-ion battery for electric vehicle applications and beyond, Energy Procedia 158 (2019) 4363–4368, innovative Solutions for Energy Transitions. doi:10.1016/j.egypro.2019.01.783.

[2] N. Wassiliadis, M. Steinsträter, M. Schreiber, P. Rosner, L. Nicoletti, F. Schmid, M. Ank, O. Teichert, L. Wildfeuer, J. Schneider, A. Koch, A. König, A. Glatz, J. Gandlgruber, T. Kröger, X. Lin, M. Lienkamp, Quantifying the state of the art of electric powertrains in battery electric vehicles: Range, efficiency, and lifetime from component to system level of the volkswagen id.3, eTransportation 12 (2022) 100167. doi:10.1016/j.etran.2022.100167.

[3] J. N. E. Lucero, V. A. Sujan, S. Onori, An experimentally validated electro-thermal ev battery pack model incorporating cycle-life aging and cell-to-cell variations, IEEE Transactions on Transportation Electrification (2024) 1–1doi:10.1109/TTE.2024.3365028.

[4] L. Chang, C. Ma, C. Zhang, B. Duan, N. Cui, C. Li, Correlations of lithium-ion battery parameter variations and connected configurations on pack statistics, Applied Energy 329 (2023) 120275. doi:10.1016/j.apenergy.2022.120275.

[5] Q. Yu, C. Wang, J. Li, R. Xiong, M. Pecht, Challenges and outlook for lithium-ion battery fault diagnosis methods from the laboratory to real

world applications, eTransportation 17 (2023) 100254. doi:10.1016/j.etran.2023.100254.

[6] Z. Li, A. Zuo, Z. Mo, M. Lin, C. Wang, J. Zhang, M. H. Hofmann, A. Jossen, Demonstrating stability within parallel connection as a basis for building large-scale battery systems, Cell Reports Physical Science 3 (12) (2022) 101154. doi:10.1016/j.xcrp.2022.101154.

[7] F. Berger, D. Joest, E. Barbers, K. Quade, Z. Wu, D. U. Sauer, P. Dechent, Benchmarking battery management system algorithms - requirements, scenarios and validation for automotive applications, eTransportation 22 (2024) 100355. doi:10.1016/j.etran.2024.100355.

[8] Q. Zhou, D. Anderson, J. Sun, State of health estimation for battery modules with parallel-connected cells under cell-to-cell variations, eTransportation 22 (2024) 100346. doi:10.1016/j.etran.2024.100346.

[9] X. Tang, Y. Zhou, F. Gao, X. Lai, Joint estimation of state-of-charge and state-of-health for all cells in the battery pack using "leader-follower" strategy, eTransportation 15 (2023) 100213. doi:10.1016/j.etran.2022.100213.

[10] M. Baumann, L. Wildfeuer, S. Rohr, M. Lienkamp, Parameter variations within li-ion battery packs – theoretical investigations and experimental quantification, Journal of Energy Storage 18 (2018) 295–307. doi:10.1016/j.est.2018.04.031.

[11] S. J. Harris, D. J. Harris, C. Li, Failure statistics for commercial lithium ion batteries: A study of 24 pouch cells, Journal of Power Sources 342 (2017) 589–597. doi:10.1016/j.jpowsour.2016.12.083.

[12] M. Dubarry, C. Pastor-Fernández, G. Baure, T. F. Yu, W. D. Widanage, J. Marco, Battery energy storage system modeling: Investigation of intrinsic cell-to-cell variations, Journal of Energy Storage 23 (2019) 19–28. doi:10.1016/j.est.2019.02.016.

[13] K. Rumpf, M. Naumann, A. Jossen, Experimental investigation of parametric cell-to-cell variation and correlation based on 1100 commercial lithium-ion cells, Journal of Energy Storage 14 (2017) 224–243. doi:10.1016/j.est.2017.09.010.

[14] L. Wildfeuer, M. Lienkamp, Quantifiability of inherent cell-to-cell variations of commercial lithium-ion batteries, eTransportation 9 (2021) 100129. doi:10.1016/j.etran.2021.100129.

[15] P. Jocher, M. Steinhardt, S. Ludwig, M. Schindler, J. Martin, A. Jossen, A novel measurement technique for parallel-connected lithium-ion cells with controllable interconnection resistance, Journal of Power Sources 503 (2021) 230030. doi:10.1016/j.jpowsour.2021.230030.

[16] M. Ank, T. Brehler, M. Lienkamp, Wire bond contact defect identification in battery modules of electric vehicles using pulses and differential voltage analysis, eTransportation 18 (2023) 100284. doi:10.1016/j.etran.2023.100284.

[17] W. Yang, M. Lang, X. Yu, X. Yang, Influence of connection impedance on the performance of parallel-connected lithium-ion battery modules, Journal of Power Sources 593 (2024) 233949. doi:10.1016/j.jpowsour.2023.233949.

[18] J. Lv, S. Lin, W. Song, M. Chen, Z. Feng, Y. Li, Y. Ding, Performance of lifepo4 batteries in parallel based on connection topology, Applied Energy 252 (2019) 113407. doi:10.1016/j.apenergy.2019.113407.

[19] E. Hosseinzadeh, S. Arias, M. Krishna, D. Worwood, A. Barai, D. Widanalage, J. Marco, Quantifying cell-to-cell variations of a parallel battery module for different pack configurations, Applied Energy 282 (2021) 115859. doi:10.1016/j.apenergy.2020.115859.

[20] Z. Zhang, Z. Li, X. Yang, J. Gong, J. Zhang, Thermal management of parallel cells — methodology based on non-linear dynamics, eTransportation 13 (2022) 100187. doi:10.1016/j.etran.2022.100187.

[21] A. Fill, K. Peter Birke, Influences of cell to cell variances and the battery design on thermal and electrical imbalances among parallel lithium-ion cells, in: 2021 22nd IEEE International Conference on Industrial Technology (ICIT), Vol. 1, 2021, pp. 391–396. doi:10.1109/ICIT46573.2021.9453477.

[22] Z. Guo, J. Xu, X. Wang, X. Mei, Fast multilayer temperature distribution estimation for lithium-ion battery pack, eTransportation 18 (2023) 100266. doi:10.1016/j.etran.2023.100266.

[23] Y. Troxler, B. Wu, M. Marinescu, V. Yufit, Y. Patel, A. J. Marquis, N. P. Brandon, G. J. Offer, The effect of thermal gradients on the performance of lithium-ion batteries, Journal of Power Sources 247 (2014) 1018–1025. doi:10.1016/j.jpowsour.2013.06.084.

[24] M. P. Klein, J. W. Park, Current distribution measurements in parallel-connected lithium-ion cylindrical cells under non-uniform temperature conditions, Journal of The Electrochemical Society 164 (9) (2017) A1893. doi:10.1149/2.0011709jes.

[25] N. Yang, X. Zhang, B. Shang, G. Li, Unbalanced discharging and aging due to temperature differences among the cells in a lithium-ion battery pack with parallel combination, Journal of Power Sources 306 (2016) 733–741. doi:10.1016/j.jpowsour.2015.12.079.

[26] S. Menner, J. Siehr, M. Buchholz, Investigation of current distributions of large-format pouch cells with individual temperature gradients by segmentation, Journal of Energy Storage 35 (2021) 102300. doi:10.1016/j.est.2021.102300.

[27] A. Fill, T. Mader, T. Schmidt, A. Avdyli, M. Kopp, K. P. Birke, Experimental investigations on current and temperature imbalances among parallel-connected lithium-ion cells at different thermal conditions, Journal of Energy Storage 51 (2022) 104325. doi:10.1016/j.est.2022.104325.

[28] M. Naylor Marlow, J. Chen, B. Wu, Degradation in parallel-connected

lithium-ion battery packs under thermal gradients, Communications Engineering 3 (1) (1 2024). doi:10.1038/s44172-023-00153-5.

[29] W. Shi, X. Hu, C. Jin, J. Jiang, Y. Zhang, T. Yip, Effects of imbalanced currents on large-format lifepo4/graphite batteries systems connected in parallel, Journal of Power Sources 313 (2016) 198–204. doi:10.1016/j.jpowsour.2016.02.087.

[30] A. Fill, S. Koch, A. Pott, K.-P. Birke, Current distribution of parallel-connected cells in dependence of cell resistance, capacity and number of parallel cells, Journal of Power Sources 407 (2018) 147–152. doi:10.1016/j.jpowsour.2018.10.061.

[31] A. Fill, S. Koch, K. P. Birke, Analytical model of the current distribution of parallel-connected battery cells and strings, Journal of Energy Storage 23 (2019) 37–43. doi:10.1016/j.est.2019.02.031.

[32] M. J. Brand, M. H. Hofmann, M. Steinhardt, S. F. Schuster, A. Jossen, Current distribution within parallel-connected battery cells, Journal of Power Sources 334 (2016) 202–212. doi:10.1016/j.jpowsour.2016.10.010.

[33] M. H. Hofmann, K. Czyrka, M. J. Brand, M. Steinhardt, A. Noel, F. B. Spingler, A. Jossen, Dynamics of current distribution within battery cells connected in parallel, Journal of Energy Storage 20 (2018) 120–133. doi:10.1016/j.est.2018.08.013.

[34] A. Fill, T. Schmidt, T. Mader, R. Llorente, A. Avdyli, K. P. Birke, New semi-analytical model approach of the current distribution within

parallel-connected lithium-ion cells, Journal of Energy Storage 40 (2021) 102653. doi:10.1016/j.est.2021.102653.

[35] D. Zhang, L. D. Couto, P. Gill, S. Benjamin, W. Zeng, S. J. Moura, Interval observer for soc estimation in parallel-connected lithium-ion batteries, in: 2020 American Control Conference (ACC), 2020, pp. 1149–1154. doi:10.23919/ACC45564.2020.9147468.

[36] R. Drummond, L. D. Couto, D. Zhang, Resolving kirchhoff's laws for parallel li-ion battery pack state-estimators, IEEE Transactions on Control Systems Technology 30 (5) (2022) 2220–2227. doi:10.1109/TCST.2021.3134451.

[37] L. Wang, Y. Xu, E. Wang, X. Zhao, S. Qiao, G. Li, H. Sun, Modeling and state of charge estimation of inconsistent parallel lithium-ion battery module, Journal of Energy Storage 51 (2022) 104565. doi:10.1016/j.est.2022.104565.

[38] C. Luan, C. Ma, C. Wang, L. Chang, L. Xiao, Z. Yu, H. Li, Influence of the connection topology on the performance of lithium-ion battery pack under cell-to-cell parameters variations, Journal of Energy Storage 41 (2021) 102896. doi:10.1016/j.est.2021.102896.

[39] X. Li, Y. Ma, A method for simplified modeling and capacity, state of charge, current distribution analysis based on arbitrary topology connection battery pack, Journal of Energy Storage 57 (2023) 106206. doi:10.1016/j.est.2022.106206.

[40] A. Fill, T. Schmidt, T. Mader, R. Llorente, A. Avdyli, B. Mulder, K. P. Birke, Influence of cell parameter differences and dynamic current stresses on the current distribution within parallel-connected lithium-ion cells, Journal of Energy Storage 32 (2020) 101929. doi:10.1016/j.est.2020.101929.

[41] Z. Song, X.-G. Yang, N. Yang, F. P. Delgado, H. Hofmann, J. Sun, A study of cell-to-cell variation of capacity in parallel-connected lithium-ion battery cells, eTransportation 7 (2021) 100091. doi:10.1016/j.etran.2020.100091.

[42] X. Zhou, S. Zhou, Z. Gao, G. Wang, L. Zong, J. Liu, F. Zhu, H. Ming, Y. Zheng, F. Chen, N. Cao, S. Yang, A statistical distribution-based pack-integrated model towards state estimation for lithium-ion batteries, eTransportation 19 (2024) 100302. doi:10.1016/j.etran.2023.100302.

[43] W. Han, F. Altaf, C. Zou, T. Wik, State of power prediction for battery systems with parallel-connected units, IEEE Transactions on Transportation Electrification 8 (1) (2022) 925–935. doi:10.1109/TTE.2021.3101242.

[44] A. Graule, F. Oehler, J. Schmitt, J. Li, A. Jossen, Development and evaluation of a physicochemical equivalent circuit model for lithium-ion batteries, Journal of The Electrochemical Society 171 (2) (2024) 020503. doi:10.1149/1945-7111/ad1ec7.

[45] S. Fasolato, A. Allam, S. Onori, D. M. Raimondo, Analyzing cell-to-

cell heterogeneities and cell configurations in parallel-connected battery modules using physics-based modeling, Journal of Energy Storage 129 (2025) 116942. doi:10.1016/j.est.2025.116942.

[46] X. Liu, W. Ai, M. Naylor Marlow, Y. Patel, B. Wu, The effect of cell-to-cell variations and thermal gradients on the performance and degradation of lithium-ion battery packs, Applied Energy 248 (2019) 489–499. doi:10.1016/j.apenergy.2019.04.108.

[47] Y. Tian, Z. Huang, X. Li, J. Tian, Parallel-connected battery module modeling based on physical characteristics in multiple domains and heterogeneous characteristic analysis, Energy 239 (2022) 122181. doi:10.1016/j.energy.2021.122181.

[48] B. Wu, V. Yufit, M. Marinescu, G. J. Offer, R. F. Martinez-Botas, N. P. Brandon, Coupled thermal–electrochemical modelling of uneven heat generation in lithium-ion battery packs, Journal of Power Sources 243 (2013) 544–554. doi:10.1016/j.jpowsour.2013.05.164.

[49] E. Hosseinzadeh, J. Marco, P. Jennings, Combined electrical and electrochemical-thermal model of parallel connected large format pouch cells, Journal of Energy Storage 22 (2019) 194–207. doi:10.1016/j.est.2019.02.004.

[50] T. G. Tranter, R. Timms, V. Sulzer, F. B. Planella, G. M. Wiggins, S. V. Karra, P. Agarwal, S. Chopra, S. Allu, P. R. Shearing, D. J. l. Brett, liionpack: A python package for simulating packs of batteries

with pybamm, Journal of Open Source Software 7 (70) (2022) 4051. doi:10.21105/joss.04051.

[51] V. Sulzer, S. G. Marquis, R. Timms, M. Robinson, S. J. Chapman, Python battery mathematical modelling (pybamm), Journal of Open Research Software (Jun 2021). doi:10.5334/jors.309.

[52] P. Rodríguez-Iturriaga, E. E. Valdés, S. Rodríguez-Bolívar, V. M. García, D. Anseán, J. A. López-Villanueva, Efficient high-fidelity modeling of a nickel-rich silicon-graphite cell enabled by optimal spatial distribution, Applied Energy 389 (2025) 125748. doi:10.1016/j.apenergy.2025.125748.

[53] O. Barcia, E. D'Elia, I. Frateur, O. Mattos, N. Pébère, B. Tribollet, Application of the impedance model of de levie for the characterization of porous electrodes, Electrochimica Acta 47 (13) (2002) 2109–2116. doi:10.1016/S0013-4686(02)00081-6.

[54] E. Barsoukov, J. R. Macdonald, Impedance spectroscopy: Theory, experiment, and applications, 3rd Edition, Vol. 1, Wiley, 2018. doi:10.1002/9781119381860.

[55] J. Moškon, M. Gaberščcek, Transmission line models for evaluation of impedance response of insertion battery electrodes and cells, Journal of Power Sources Advances 7 (2021) 100047. doi:10.1016/j.powera.2021.100047.

[56] T. F. Fuller, M. Doyle, J. Newman, Simulation and Optimization of the

Dual Lithium Ion Insertion Cell, J. Electrochem. Soc. 141 (1) (1994) 1–10. doi:10.1149/1.2054684.

[57] T. F. Fuller, M. Doyle, J. Newman, Relaxation phenomena in lithium-ion-insertion cells, Journal of The Electrochemical Society 141 (4) (1994) 982. doi:10.1149/1.2054868.

[58] Y. Li, M. Vilathgamuwa, T. Farrell, S. S. Choi, N. T. Tran, J. Teague, A physics-based distributed-parameter equivalent circuit model for lithium-ion batteries, Electrochimica Acta 299 (2019) 451–469. doi:10.1016/j.electacta.2018.12.167.

[59] C.-H. Chen, F. B. Planella, K. O'Regan, D. Gastol, W. D. Widanage, E. Kendrick, Development of experimental techniques for parameterization of multi-scale lithium-ion battery models, Journal of The Electrochemical Society 167 (8) (2020) 080534. doi:10.1149/1945-7111/ab9050.

[60] C. Wang, V. Srinivasan, Computational battery dynamics (cbd)—electrochemical/thermal coupled modeling and multi-scale modeling, Journal of Power Sources 110 (2) (2002) 364–376. doi:10.1016/S0378-7753(02)00199-4.

[61] P. Rodríguez-Iturriaga, D. Anseán, S. Rodríguez-Bolívar, V. M. García, M. González, J. A. López-Villanueva, Modeling current-rate effects in lithium-ion batteries based on a distributed, multi-particle equivalent circuit model, Applied Energy 353 (2024) 122141. doi:10.1016/j.apenergy.2023.122141.

[62] P. Rodríguez-Iturriaga, V. M. García, S. Rodríguez-Bolívar, E. E. Valdés, D. Anseán, J. A. López-Villanueva, A coupled electrothermal lithium-ion battery reduced-order model including heat generation due to solid diffusion, Applied Energy 367 (2024) 123327. doi:10.1016/j.apenergy.2024.123327.

[63] W. Ai, N. Kirkaldy, Y. Jiang, G. Offer, H. Wang, B. Wu, A composite electrode model for lithium-ion batteries with silicon/graphite negative electrodes, Journal of Power Sources 527 (2022) 231142. doi:10.1016/j.jpowsour.2022.231142.

[64] T. L. Kirk, A. Lewis-Douglas, D. Howey, C. P. Please, S. J. Chapman, Nonlinear electrochemical impedance spectroscopy for lithium-ion battery model parameterization, Journal of The Electrochemical Society 170 (1) (2023) 010514. doi:10.1149/1945-7111/acada7.

[65] S. G. Marquis, V. Sulzer, R. Timms, C. P. Please, S. J. Chapman, An Asymptotic Derivation of a Single Particle Model with Electrolyte, Journal of The Electrochemical Society 166 (15) (2019) A3693–A3706. doi:10.1149/2.0341915jes.

[66] L. Parrilla, P. Rodríguez-Iturriaga, J. A. López-Villanueva, S. Rodríguez-Bolívar, E. Castillo, A. García, Towards efficient hardware digital twins of lithium-ion batteries, in: 2024 39th Conference on Design of Circuits and Integrated Systems (DCIS), 2024, pp. 1–6. doi:10.1109/DCIS62603.2024.10769206.

[67] G. Piombo, S. Fasolato, R. Heymer, M. F. Hidalgo, M. Faraji Niri,

D. M. Raimondo, J. Marco, S. Onori, "full factorial design of experiments dataset for parallel-connected lithium-ion cells imbalanced performance investigation", Data in Brief 53 (2024) 110227. doi:10.1016/j.dib.2024.110227.

[68] G. Piombo, S. Fasolato, R. Heymer, M. Hidalgo, M. Faraji Niri, S. Onori, J. Marco, Unveiling the performance impact of module level features on parallel-connected lithium-ion cells via explainable machine learning techniques on a full factorial design of experiments, Journal of Energy Storage 84 (2024) 110783. doi:10.1016/j.est.2024.110783.

[69] D. Anseán, G. Baure, M. González, I. Cameán, A. García, M. Dubarry, Mechanistic investigation of silicon-graphite/lini0.8mn0.1co0.1o2 commercial cells for non-intrusive diagnosis and prognosis, Journal of Power Sources 459 (2020) 227882. doi:10.1016/j.jpowsour.2020.227882.

[70] N. Kirkaldy, M. A. Samieian, G. J. Offer, M. Marinescu, Y. Patel, Lithium-ion battery degradation: Comprehensive cycle ageing data and analysis for commercial 21700 cells, Journal of Power Sources 603 (2024) 234185. doi:10.1016/j.jpowsour.2024.234185.

[71] J. Schmitt, M. Schindler, A. Oberbauer, A. Jossen, Determination of degradation modes of lithium-ion batteries considering aging-induced changes in the half-cell open-circuit potential curve of silicon–graphite, Journal of Power Sources 532 (2022) 231296. doi:10.1016/j.jpowsour.2022.231296.

[72] M. Fath, P. Heidebrecht, C. Drechsler, M. Kamlah, Impact of particle

size distribution on the rest phase behavior of lib cathodes – model based analysis, Journal of Power Sources 596 (2024) 234100. doi:10.1016/j.jpowsour.2024.234100.

[73] B. K. Kanchan, P. R. Randive, Implication of non-uniform anode particle morphology on lithium-ion cell performance, Journal of the Electrochemical Society 168 (5) (2021). doi:10.1149/1945-7111/ac035a.

[74] J. Zhu, X. Lai, Z. Zhu, P. Ke, Y. Zheng, X. Tang, X. Li, Y. Yuan, H. Chong, C. Yan, Y. Wang, Y. Lin, X. Zhou, Y. Chen, Online generation of full-frequency electrochemical impedance spectra for lithium-ion batteries using early-stage partial relaxation voltage curve, eTransportation 26 (2025) 100482. doi:10.1016/j.etran.2025.100482.

[75] H. Ruan, J. V. Barreras, T. Engstrom, Y. Merla, R. Millar, B. Wu, Lithium-ion battery lifetime extension: A review of derating methods, Journal of Power Sources 563 (2023) 232805. doi:10.1016/j.jpowsour.2023.232805.

[76] Faraday-Institution, An example of how to run pybamm in simulink. URL https://github.com/FaradayInstitution/pybamm_simulink_example

Highlights:

- Physically motivated efficient simulation framework for parallel-connected cells
- Determination of a cell's electrically consistent equivalent voltage and resistance
- Accurate results for module voltage (<20mV RMS) and current distribution (<4.4% RMS)
- Experimental validation covering a wide range of operating scenarios
- Improved consistency and computational cost with respect to established approaches

Declaration of interests

☒ The authors declare that they have no known competing financial interests or personal relationships that could have appeared to influence the work reported in this paper.

☐ The authors declare the following financial interests/personal relationships which may be considered as potential competing interests: